


# Octahedral rotations in Ruddlesden-Popper layered oxides under pressure from first principles

Sriram P. Ramkumar<sup>1,2</sup> and Elizabeth A. Nowadnick<sup>1,\*</sup>

<sup>1</sup>Department of Materials Science and Engineering, University of California, Merced, California 95343, USA

<sup>2</sup>Department of Physics, New Jersey Institute of Technology, Newark, New Jersey 07102, USA

 (Received 24 May 2021; revised 24 August 2021; accepted 28 September 2021; published 12 October 2021)

The combination of reduced dimensionality and tunable structural distortions in layered perovskite oxides makes these materials ideal platforms for designing novel properties and functionalities. One example is hybrid improper ferroelectricity in  $n = 2$  Ruddlesden-Popper oxides, where the combination of a layered crystal structure and rotations of the metal-oxide octahedra break symmetry and induce a polarization. Precisely controlling the octahedral rotation distortions, for example by the application of hydrostatic pressure, provides a pathway to tune and optimize the properties of these materials. We combine group theoretic methods, density functional theory calculations, and Landau theory analysis to investigate how octahedral rotations respond to pressure in the hybrid improper ferroelectrics  $\text{Sr}_3\text{Zr}_2\text{O}_7$ ,  $\text{Ca}_3\text{Ti}_2\text{O}_7$ , and  $\text{Sr}_3\text{Sn}_2\text{O}_7$ . We find that factors that are known to control the pressure response of  $\text{ABO}_3$  perovskites—the formal charge of the  $A$ - and  $B$ -site cations, tolerance factor, and  $B$ -site chemistry—also impact the pressure response of these layered perovskites. We also show that coupling between the octahedral rotation and strain order parameters plays a key role in determining the overall pressure response. Despite some similarities, we find that these layered perovskites display a distinct pressure response compared to their  $\text{ABO}_3$  perovskite analogs. By identifying trends and underlying mechanisms that control octahedral rotations in Ruddlesden-Popper oxides under pressure, this work lays the foundation for tailoring the structure and properties of these materials.

DOI: [10.1103/PhysRevB.104.144105](https://doi.org/10.1103/PhysRevB.104.144105)

## I. INTRODUCTION

Perovskite and layered perovskite oxides are a scientifically and technologically important class of materials that display a huge range of properties including ferroelectricity, superconductivity, and metal-insulator transitions. The basic structural building blocks of these materials are corner-connected  $\text{BO}_6$  octahedra. In the ideal high-symmetry structure, the  $B$ - $O$ - $B$  bond angles are  $180^\circ$ ; however, most perovskites crystallize in lower symmetry distorted structures. Octahedral rotation distortions—where the  $\text{BO}_6$  octahedra rotate about one or more crystallographic axes—are the most common type of structural distortion in perovskite oxides [1], and they couple closely to the electronic [2–4] and magnetic [5,6] properties. Controlling octahedral rotations via chemical substitution, hydrostatic pressure, and epitaxial strain in thin films provides an opportunity to design perovskites with targeted properties [4,7,8].

Several studies have explored pressure-induced changes to octahedral rotations in  $\text{ABO}_3$  perovskites [9–12]. These works have revealed that the formal charges of the  $A$ - and  $B$ -site cations provide a useful descriptor for predicting the pressure response. The formal charges can be linked to the relative compressibility of the  $\text{AO}_{12}$  and  $\text{BO}_6$  polyhedra, with a lower formal charge being associated with a more compressible polyhedron. Since the  $\text{BO}_6$  octahedra rotate fairly rigidly, the octahedral rotations primarily compress bonds in

the  $\text{AO}_{12}$  polyhedron. As a result, if the formal charge of the  $A$  cation is smaller ( $\text{A}^{2+}\text{B}^{4+}\text{O}_3$  and  $\text{A}^{1+}\text{B}^{5+}\text{O}_3$ ), the  $\text{AO}_{12}$  polyhedron is more compressible, resulting in an increase of the octahedral rotations with pressure. In contrast, when the  $A$  and  $B$  cations have the same formal charge ( $\text{A}^{3+}\text{B}^{3+}\text{O}_3$ ), the octahedral rotations decrease under pressure. The pressure response of most  $\text{ABO}_3$  perovskites can be predicted from their formal charges; however, there are exceptions such as  $\text{CaSiO}_3$  [13] and  $\text{RBO}_3$  [12,14,15] ( $R$  = rare earth;  $B$  = Al, Fe, Cr). For these cases, the  $d$ -orbital occupancy on the  $B$  site is an important factor [12].

Similar to perovskites, most layered perovskites crystallize in distorted structures with octahedral rotations. One example is the  $\text{A}_{n+1}\text{B}_n\text{O}_{3n+1}$  Ruddlesden-Popper (RP) family, where the crystal structure is built from blocks containing  $n$  perovskite layers separated by a rocksalt layer. Octahedral rotations in RPs are of particular interest because they can facilitate functionalities that do not occur in  $\text{ABO}_3$  perovskites, such as hybrid improper ferroelectricity in  $n = 2$  RPs where the electrical polarization is induced by a coupling to octahedral rotations [16–21]. Whereas there have been some studies of the effect of chemical substitution [22–27] and epitaxial strain [28,29] on octahedral rotations in RPs, the impact of hydrostatic pressure on octahedral rotations in  $n = 2$  RPs has received minimal attention.

In this work, we combine group theoretic analysis, density functional theory (DFT) calculations, and Landau theory to investigate the pressure response of a family of hybrid improper ferroelectric  $n = 2$  RP materials:  $\text{Sr}_3\text{Zr}_2\text{O}_7$  [18],  $\text{Ca}_3\text{Ti}_2\text{O}_7$  [21,30], and  $\text{Sr}_3\text{Sn}_2\text{O}_7$  [17,20,31]. By investigating

\*enowadnick@ucmerced.edu

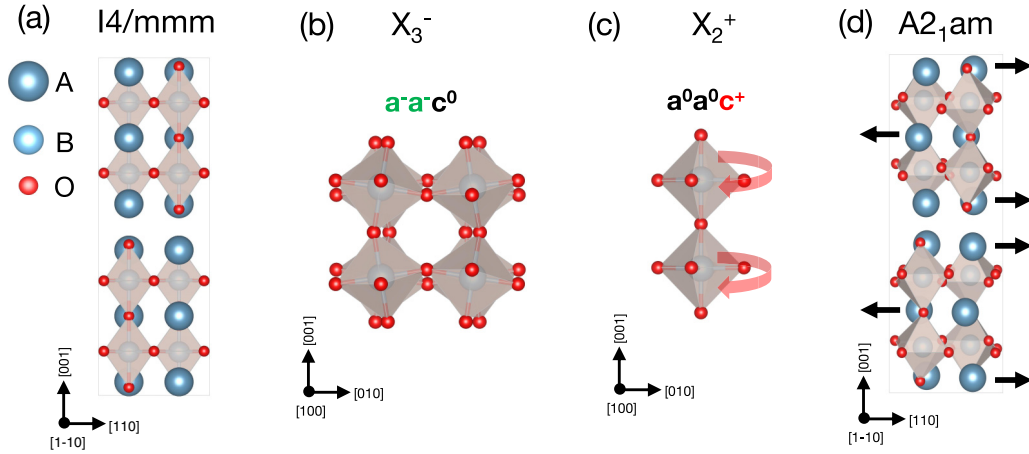


FIG. 1. Crystal structure of  $n = 2$  Ruddlesden-Popper  $A_3B_2O_7$  materials. (a) The high-symmetry reference structure  $I4/mmm$ , which consists of two perovskite slabs separated by a rocksalt layer. The condensation of two octahedral rotations establishes the polar  $A2_1am$  structure: (b) an out-of-phase ( $a^-a^-c^0$ ) octahedral rotation about  $[110]$  which transforms like  $X_3^-$  and (c) an in-phase ( $a^0a^0c^+$ ) octahedral rotation about  $[001]$  which transforms like  $X_2^+$ . The  $A2_1am$  ground state structure is shown in (d). The black arrows show the two-against-one A-site displacements along  $[110]$  in each perovskite slab, which are the main contribution to the polarization. In all panels, the axes of the tetragonal cell are shown.

several structural phases of these materials under pressure, we observe a distinct response depending on whether one or more octahedral rotations distort the crystal structure. For single-rotation structures, the octahedral rotation amplitudes generally increase with pressure, in agreement with the perovskite formal charge descriptor (the charges on the A and B cations are 2+ and 4+, respectively, for all materials that we consider). In some cases, we find that the tolerance factor and B-site chemistry also play a role. In contrast, we find that the pressure response of the ground state  $A2_1am$  ferroelectric phase of these materials—where two octahedral rotations and a polar distortion are coupled together—is not adequately described by the formal charge descriptor. To understand this, we perform and analyze a Landau free energy expansion including both the structural distortion order parameters and strain modes. We find that distinct strain states realized in the single- and multirotation structures are the primary reason for their different pressure responses. Throughout, we discuss differences and similarities between the pressure response of the RPs and their  $ABO_3$  perovskite analogs.

## II. METHODS

We perform DFT [32] calculations using VASP [33] and the projector augmented wave (PAW) [34] method. We adopt the PBEsol version of the Perdew-Burke-Ernzerhof (PBE) exchange-correlation functional [35]. The atomic positions and lattice vectors are optimized with a convergence criteria on the total energy of  $10^{-8}$  eV and 2 meV/Å on the forces. For all calculations, a kinetic energy cutoff of 600 eV is employed for truncating the plane wave basis set. The Brillouin zone is sampled using a  $6 \times 6 \times 2$  Monkhorst-Pack [36]  $k$ -point mesh in a 48-atom computational cell. We use the standard VASP pseudopotentials with the following valence states for our computations: Ca\_pv ( $3p^64s^2$ ), Sr\_sv ( $4s^24p^65s^2$ ), Ba\_sv ( $5s^25p^66s^2$ ), Ti\_pv ( $3p^63d^34s^1$ ), Zr\_sv ( $4s^25s^14p^64d^3$ ), Sn\_d ( $4d^{10}5s^25p^2$ ), and O ( $2s^22p^4$ ). We make use of the ISOTROPY

software suite [37] for group theoretic analysis and VESTA [38] for the visualization of crystal structures.

## III. GROUND STATE STRUCTURES

At room temperature,  $Ca_3Ti_2O_7$ ,  $Sr_3Zr_2O_7$ , and  $Sr_3Sn_2O_7$  all crystallize in the orthorhombic polar space group  $A2_1am$  [18,20,21]. This structure can be decomposed into three structural distortions which transform like irreducible representations (irreps) of the high-symmetry reference structure  $I4/mmm$ , shown in Fig. 1(a). These distortions, shown in Figs. 1(b)–1(d), are an out-of-phase ( $a^-a^-c^0$  in Glazer notation [39]) octahedral rotation about  $[110]$  which transforms like the irrep  $X_3^-$ , an in-phase ( $a^0a^0c^+$ ) octahedral rotation about  $[001]$  transforming like  $X_2^+$ , and a polar distortion primarily involving A-site displacements which transforms like  $\Gamma_5^-$ . The amplitudes of these distortions, obtained from structural decompositions of DFT-relaxed structures, are shown in Table I.

The distortion amplitudes of  $Sr_3Sn_2O_7$  are smaller than those of  $Ca_3Ti_2O_7$  and  $Sr_3Zr_2O_7$ . This is expected because, as shown in Table I, the tolerance factor [40]  $\tau = (r_A + r_O)/[\sqrt{2}(r_B + r_O)]$  of the corresponding perovskite ( $SrSnO_3$ ), which also is predictive of octahedral rotation amplitudes in RPs [41], is the largest (closest to 1).

## IV. PRESSURE RESPONSE OF SINGLE-ROTATION RP STRUCTURES

We first consider the pressure response of RP structures that are characterized by a single octahedral rotation distortion. These structures are simpler than  $A2_1am$ , where the three active structural distortions described above are coupled together. We focus on the same set of materials ( $Sr_3Zr_2O_7$ ,  $Ca_3Ti_2O_7$ , and  $Sr_3Sn_2O_7$ ), and constrain their symmetries to single-rotation phases. These include a structure with only the  $a^-a^-c^0$  octahedral rotation (transforming like  $X_3^-$ ), which has

TABLE I. Perovskite tolerance factors [40] calculated using the bond-valence model [42–44], amplitudes of the  $X_2^+$ ,  $X_3^-$ , and  $\Gamma_5^-$  distortions, and lattice parameters (in Å) of the DFT-relaxed  $A2_1am$  structure. The distortion amplitudes are obtained by decomposing the  $A2_1am$  structure into symmetry adapted modes of the high-symmetry  $I4/mmm$  references structure, and are reported in units of Å for a 48-atom cell.

Material	$t_{bv}$	$X_2^+$	$X_3^-$	$\Gamma_5^-$	$a$	$b$	$c$
$\text{Sr}_3\text{Zr}_2\text{O}_7$	0.942	1.23	1.80	0.75	5.809	5.801	20.797
$\text{Ca}_3\text{Ti}_2\text{O}_7$	0.946	1.26	1.76	0.89	5.447	5.384	19.266
$\text{Sr}_3\text{Sn}_2\text{O}_7$	0.957	1.09	1.66	0.64	5.753	5.743	20.623

symmetry  $Amam$ , and a structure with only the  $a^0a^0c^+$  octahedral rotation (transforming like  $X_2^+$ ), which has symmetry  $Acam$ . We also consider a structure with a single  $a^0a^0c^-$  rotation that transforms like  $X_1^-$  (symmetry  $Acaa$ ). We consider  $Acaa$  because phases with  $a^0a^0c^-$  rotations have been found at elevated temperatures and are predicted in epitaxially strained thin films of  $n = 2$  RPs [17,28].

A second set of single-rotation structures can be generated by rotating the two-dimensional octahedral rotation order parameters [45] by  $45^\circ$ . For the case of the  $X_3^-$  octahedral rotation, this structure has symmetry  $P4_2/mnm$  (with octahedral rotations about the [100] and [010] axes in alternating perovskite slabs). The  $P4_2/mnm$  phase has been observed experimentally in several  $n = 2$  RP materials with larger tolerance factors, including  $\text{Ca}_2\text{SrTi}_2\text{O}_7$  [46–48]. We do not consider the structures arising from rotation of the  $X_2^+$  and  $X_1^-$  order parameters (symmetry  $P4/mbm$  and  $P4/nbm$ , respectively), because they are much higher in energy [45]. The total energies and structural decompositions of our DFT-relaxed single-rotation structures at zero pressure are reported in Appendix A.

We then use DFT to relax these single-rotation structures under hydrostatic pressure and obtain their octahedral rotation amplitudes, as shown in Fig. 2. The  $X_3^-$  rotations in Fig. 2(a) increase with pressure in  $\text{Sr}_3\text{Zr}_2\text{O}_7$  and  $\text{Ca}_3\text{Ti}_2\text{O}_7$ , whereas they decrease slightly in  $\text{Sr}_3\text{Sn}_2\text{O}_7$ . The pressure responses

of the  $Amam$  and  $P4_2/mnm$  structures are very similar. For all three compounds, the  $X_2^+$  and  $X_1^-$  rotations increase with pressure [Figs. 2(b) and 2(c)] and their rate of increase is large compared to that of  $X_3^-$ . With the exception of the  $X_3^-$  rotation in  $\text{Sr}_3\text{Sn}_2\text{O}_7$ , the pressure response of the single-rotation RP structures aligns with the prediction of the perovskite formal charge descriptor for compounds with  $A^{2+}$  and  $B^{4+}$  cations [11].

To understand why the behavior of the  $\text{Sr}_3\text{Sn}_2\text{O}_7$   $X_3^-$  rotation deviates from the formal charge descriptor, we first note that previous studies of  $\text{ABO}_3$  perovskites have found that both tolerance factor and the  $B$ -site chemistry also impact the pressure response [12]. As noted above,  $\text{Sr}_3\text{Sn}_2\text{O}_7$  has the largest (closest to 1) tolerance factor of the compounds that we consider. Also, Sn is a  $p$ -block element, whereas Ti and Zr lie in the  $d$  block. Depending on whether the  $B$  cation lies in the  $p$  or  $d$  block, the  $B$ -O bonding has different character (relative contributions of  $\sigma$  and  $\pi$  bonding), which favors different  $B$ -O-B bond angles [1].

To investigate whether tolerance factor and  $B$ -site chemistry play a role in determining the pressure response of RPs, we expand our family of materials by keeping the same  $B$ -site cations (Zr, Ti, Sn), but placing different combinations of Ca, Sr, and Ba on the  $A$  sites. The  $n = 2$  RP structure has two crystallographically distinct  $A$  sites:  $A_P$ , which lies in the center of the perovskite layer, and  $A_{RS}$  which borders the

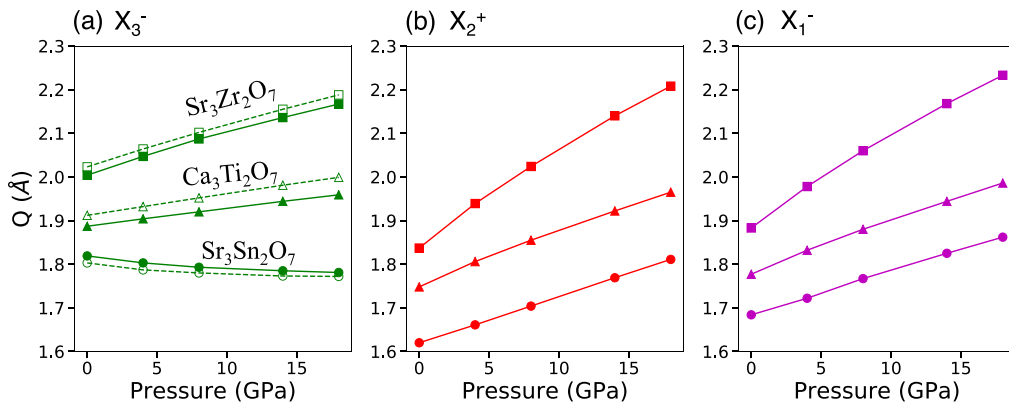


FIG. 2. Pressure dependence of  $n = 2$  Ruddlesden-Popper structures with single octahedral rotation distortions. (a) Octahedral rotation amplitudes ( $Q$ ) as a function of pressure for structures with symmetry  $Amam$  (filled markers) and  $P4_2/mnm$  (empty markers). The octahedral rotations in both structures transform like  $X_3^-$ ; in  $Amam$  the rotation pattern is  $a^-a^-c^0$  in all perovskite slabs, whereas in  $P4_2/mnm$  it is  $a^-b^0b^0/b^0a^-b^0$  in alternating slabs. (b) Pressure dependence of the  $X_2^+$  ( $a^0a^0c^+$ ) octahedral rotation in the  $Acam$  structure and (c) pressure dependence of the  $X_1^-$  ( $a^0a^0c^-$ ) octahedral rotation in the  $Acaa$  structure. In all panels, results for  $\text{Sr}_3\text{Zr}_2\text{O}_7$ ,  $\text{Ca}_3\text{Ti}_2\text{O}_7$ , and  $\text{Sr}_3\text{Sn}_2\text{O}_7$  are denoted by squares, triangles, and circles, respectively. The distortion amplitudes are given for a 48 atom cell and are computed by decomposing the distorted structures with respect to  $I4/mmm$  relaxed at the same pressure.

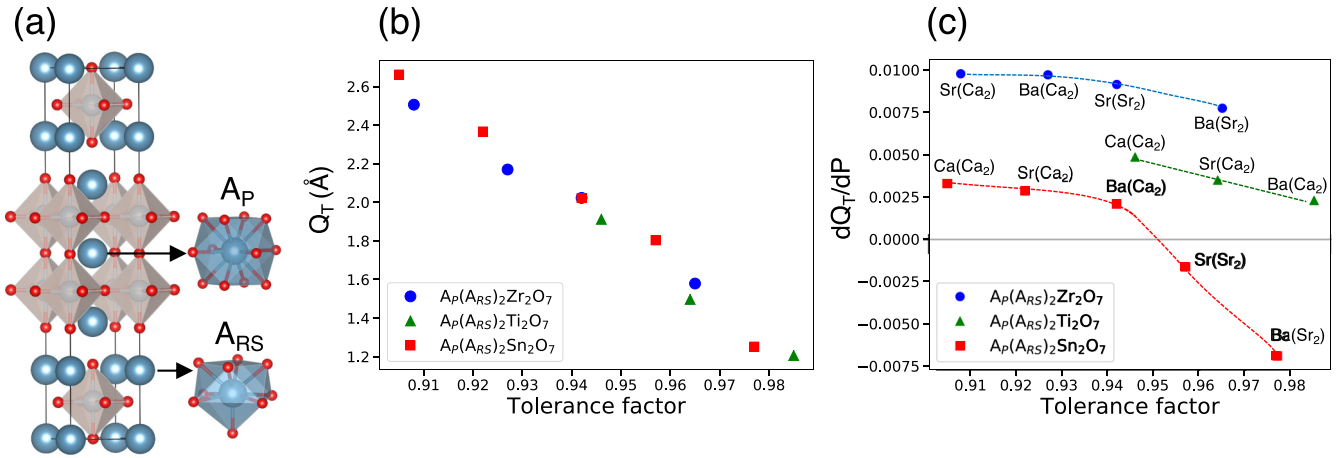


FIG. 3. Pressure dependence of the  $P4_2/mmm$  structure with mixed  $A$ -site cations. (a) The two crystallographically distinct  $A$  sites in the  $A_3B_2O_7$  structure: a larger 12-fold coordinated site in the center of the perovskite double layer ( $A_P$ ) and a smaller 9-fold coordinated site bordering the rocksalt layer ( $A_{RS}$ ). (b)  $X_3^-$  octahedral rotation amplitude ( $Q_T$ ) at 0 GPa as a function of tolerance factor and (c) change in rotation amplitude with respect to pressure ( $dQ_T/dP$ ) for a series of  $A_P(A_{RS})_2B_2O_7$  compounds ( $B = Zr, Ti, Sn$ ). The  $A$ -site cations (Ca, Sr, Ba) are indicated in panel (c) and the dashed lines in (c) are guides to the eye. The derivative  $dQ_T/dP$  shown in panel (c) is given in units of  $\text{\AA}/\text{GPa}$ .

rocksalt layer [Fig. 3(a)]. Here, we consider  $A$ -site ordered RPs  $A_P(A_{RS})_2B_2O_7$ , where we place the larger of the two cations on the  $A_P$  site which has a larger size. Restricting our investigation to the  $P4_2/mmm$  structure, we then perform DFT calculations on our expanded family of materials. Figure 3(b) shows the zero-pressure  $X_3^-$  rotation amplitude as a function of tolerance factor for our expanded set of compounds. For the mixed  $A$ -site compounds, we compute the tolerance factor as a weighted average:  $\tau = (1/3)\tau_{A_PBO_3} + (2/3)\tau_{A_{RS}BO_3}$  [49]. We find that, as expected, the octahedral rotation amplitude monotonically increases as the tolerance factor decreases.

We next consider the pressure response of this expanded family of materials. Figure 3(c) shows the rate of change of the  $X_3^-$  octahedral rotation amplitude  $Q_T$  with pressure ( $dQ_T/dP$ ), obtained by fitting the slope of a  $Q_T$  vs pressure plot for each material (see Appendix A). Figure 3(c) enables several interesting observations. First, we observe that the materials naturally group based on their  $B$  site, where for a given tolerance factor  $dQ_T/dP$  is largest for the Zr-based materials and smallest for the Sn-based materials. For all  $B$  sites, we find that  $dQ_T/dP$  decreases as the tolerance factor increases, which is consistent with the behavior of perovskites [12]. All compounds have positive  $dQ_T/dP$  values with the exception of  $Sr_3Sn_2O_7$  and  $BaSr_2Sn_2O_7$ . Based on the trends in Fig. 3(c), we expect that Zr- and Ti-based materials with larger tolerance factors also could show a crossover to a negative  $dQ_T/dP$ . In practice, however, the rotation may disappear as the tolerance factor gets close to 1 before this crossover is observed. We thus find that, in analogy with  $ABO_3$  perovskites, both  $B$ -site chemistry and tolerance factor influence the pressure response.

However, the pressure response of the RPs is not completely analogous with that of the corresponding perovskite. To show this, we compute the pressure response of perovskite  $SrSnO_3$  when it is constrained to structural phases with a single  $a^-a^-c^0$  rotation (space group  $Imma$ ) and a single  $a^0a^0c^+$  rotation (space group  $P4/mbm$ ). As shown in Appendix B,

we find that both octahedral rotation amplitudes increase with pressure, adhering with the perovskite formal charge descriptor. This observation then suggests that an aspect of the  $n = 2$  RP structure itself plays a role in the  $Sr_3Sn_2O_7$  pressure response. We hypothesize that this could be the different bonding preferences of the  $A_P$  and  $A_{RS}$  sites, where the larger  $A_P$  site is more underbonded than the  $A_{RS}$  site. This can be quantified by computing the bond valences, which for  $Sr_3Sn_2O_7$  in the  $I4/mmm$  structure are 1.614 and 1.752 for  $A_P$  and  $A_{RS}$ , respectively. Since the optimization of  $A-O$  bonding is a main factor driving octahedral rotations [1], this difference in bond valence implies that the  $A_P$  cation “wants” a larger octahedral rotation amplitude than the  $A_{RS}$  cations to satisfy its bonding. The resulting octahedral rotation amplitude and its pressure response would be a compromise between the two.

To summarize this section, we find that the pressure response of  $A_3^{2+}B_2^{4+}O_7$  RPs is mostly captured by the perovskite formal charge descriptor. The tolerance factor and the chemistry of the  $B$  cation also plays a role in determining the magnitude of the response. However, the behavior of the RP is not always in analogy with that of the corresponding perovskite, an effect that we attribute to the competing bonding preferences of the two distinct  $A$ -cation sites in the RP structure.

## V. PRESSURE RESPONSE OF THE POLAR $A2_1am$ STRUCTURE

We next explore the pressure response of the ground state  $A2_1am$  structure. Figure 4 shows the pressure evolution of the three active structural distortions ( $X_3^-$  rotation,  $X_2^+$  rotation, and  $\Gamma_5^-$  polar mode). The most noticeable feature compared to the single-rotation structures (Fig. 2) is that both the distortion amplitudes  $Q$  and their rate of change with pressure  $dQ/dP$  are significantly smaller. This effect is most noticeable for the  $X_2^+$  rotation. Furthermore, contrasting with the single-rotation case, where all distortions (except for the  $X_3^-$  rotation

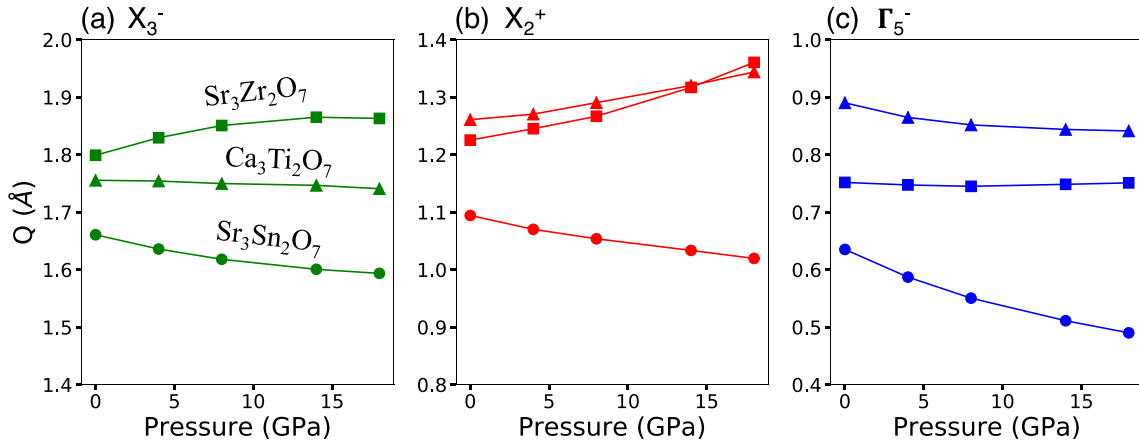


FIG. 4. Pressure dependence of structural distortion amplitudes ( $Q$ ) contributing to the  $A2_1am$  structure: (a)  $X_3^-$  rotation, (b)  $X_2^+$  rotation, and (c)  $\Gamma_5^-$  polar distortion for  $\text{Sr}_3\text{Zr}_2\text{O}_7$  (squares),  $\text{Ca}_3\text{Ti}_2\text{O}_7$  (triangles), and  $\text{Sr}_3\text{Sn}_2\text{O}_7$  (circles). The amplitudes are reported for a 48 atom computational cell.

in  $\text{Sr}_3\text{Sn}_2\text{O}_7$ ) increased with pressure, the pressure response of the  $A2_1am$  structure is more varied. First considering the  $X_3^-$  rotation [Fig. 4(a)], as pressure increases its amplitude increases for  $\text{Sr}_3\text{Zr}_2\text{O}_7$ , whereas it decreases for  $\text{Sr}_3\text{Sn}_2\text{O}_7$  and  $\text{Ca}_3\text{Ti}_2\text{O}_7$  (very slightly, in the latter case). Next considering the  $X_2^+$  rotation [Fig. 4(b)], it increases with pressure for  $\text{Sr}_3\text{Zr}_2\text{O}_7$  and  $\text{Ca}_3\text{Ti}_2\text{O}_7$ , and decreases for  $\text{Sr}_3\text{Sn}_2\text{O}_7$ . Finally, the  $\Gamma_5^-$  polar distortion [Fig. 4(c)] decreases for all three compounds, albeit very slightly for  $\text{Sr}_3\text{Zr}_2\text{O}_7$ . We note that this decrease in polar distortion amplitude contrasts with recent reports of polarization enhancement under pressure for some  $\text{ABO}_3$  perovskites [50,51]. This difference is likely due to the fact that the polarization is induced by a trilinear coupling in the  $n = 2$  RPs that we study, rather than a polar instability.

To start understanding why each of the three  $A2_1am$  RP compounds displays a distinct pressure response, we first compare to the corresponding  $\text{ABO}_3$  perovskite materials ( $\text{SrZrO}_3$ ,  $\text{CaTiO}_3$ , and  $\text{SrSnO}_3$ ). The ground state structure of these perovskites has symmetry  $Pbnm$ , which can be thought of as analogous to the  $A2_1am$  RP structure, in that it contains an out-of-phase ( $a^-a^-c^0$ ) octahedral rotation, an in-phase ( $a^0a^0c^+$ ) octahedral rotation, and an antipolar (rather than polar) displacement mode coupled together by a trilinear term. Computing the pressure dependence of the distortion amplitudes (Appendix B), we find that, similar to the RPs, both the rotation amplitudes and their rate of change are suppressed compared to the single-rotation case. However, in contrast with the RPs, the amplitudes increase with pressure for all materials (as expected based on the formal charge descriptor). Therefore, whereas  $\text{Sr}_3\text{Zr}_2\text{O}_7$  and  $\text{SrZrO}_3$  exhibit a similar pressure response (all modes increase), both  $\text{Ca}_3\text{Ti}_2\text{O}_7$  and  $\text{Sr}_3\text{Sn}_2\text{O}_7$  display distinct pressure responses from their perovskite analogs.

As discussed in Sec. IV, the tolerance factor and  $B$ -site chemistry provide a useful way to organize the pressure response for the single-rotation structures. To assess whether this is also the case for the  $A2_1am$  structure, we compute the derivatives of the  $X_3^-$  and  $X_2^+$  octahedral rotation amplitudes with respect to pressure ( $dQ_T/dP$  and  $dQ_R/dP$ ) in Appendix C for an expanded family of compounds. We find

that  $dQ_T/dP$  displays a similar trend with tolerance factor as the single-rotation case shown in Fig. 2(c). In contrast, we see no clear dependence of  $dQ_R/dP$  on the tolerance factor. In addition, we do not observe a clear grouping of compounds based on their  $B$ -site chemistry, either. This suggests that additional factors play a key role in the  $A2_1am$  pressure response, which we explore in the next sections. As we will show below, the key difference between the single-rotation structures and  $A2_1am$  is the role that strain modes play in determining the octahedral rotation amplitudes.

## VI. LANDAU FREE ENERGY EXPANSION

We start by writing down a Landau free energy expansion about the high-symmetry reference  $I4/mmm$  for a single-rotation phase (we take the example of a structure with a single  $X_3^-$  rotation of amplitude  $Q_T$ ):

$$E(Q_T) = \alpha_T Q_T^2 + \beta_T Q_T^4. \quad (1)$$

The octahedral rotation  $Q_T$  also couples to the strain of the unit cell. Here the strain along lattice parameter  $a$  of a distorted structure is  $(a - a_0)/a_0$ , where  $a_0$  is the corresponding lattice parameter of the  $I4/mmm$  structure. We choose to decompose the strain into components that emphasize the tetragonal and orthorhombic deformations of the unit cell: two strain modes that cause a tetragonal distortion with symmetry  $\Gamma_1^+$  that correspond to stretching in the  $ab$  plane and along  $c$  (we denote these by  $\eta_{xx}$  and  $\eta_z$ , respectively), and one with symmetry  $\Gamma_4^+$  which produces the orthorhombic distortion of the unit cell ( $\eta_o$ ). The coupling between  $Q_T$  and strain can then be written as

$$E_{Q\eta}(Q_T, \eta) = (\gamma \cdot \eta) Q_T^2, \quad (2)$$

where  $\gamma = (\gamma_1, \gamma_2, \gamma_3)$  are the Landau coefficients and  $\eta = (\eta_{xx}, \eta_z, \eta_o)$  is the strain.

The amplitude of  $Q_T$  that minimizes the energy is

$$Q_T = \sqrt{\frac{-\alpha_T - (\gamma \cdot \eta)}{2\beta_T}}. \quad (3)$$

A key difference between the  $A2_1am$  and single-rotation structures is the presence of coupling terms between the structural distortion order parameters. In this case, the Landau expansion becomes

$$E(Q_T, Q_R, Q_P) = \alpha_R Q_R^2 + \beta_R Q_R^4 + \alpha_T Q_T^2 + \beta_T Q_T^4 + \alpha_P Q_P^2 + \beta_P Q_P^4 + \lambda Q_R Q_T Q_P + \delta_{RT} Q_R^2 Q_T^2 + \delta_{RP} Q_R^2 Q_P^2 + \delta_{TP} Q_T^2 Q_P^2. \quad (4)$$

Here,  $Q_T$ ,  $Q_R$ , and  $Q_P$  denote the amplitudes of the  $X_3^-$ ,  $X_2^+$ , and  $\Gamma_5^-$  distortions, respectively.

Each structural distortion order parameter also couples to the strain modes:

$$E_{Q\eta} = (\gamma_T \cdot \eta) Q_T^2 + (\gamma_R \cdot \eta) Q_R^2 + (\gamma_P \cdot \eta) Q_P^2, \quad (5)$$

where  $\gamma_i$  are the coefficients for distortion  $i$  and  $\eta$  is defined as above. We make use of the Landau expansion introduced here in the analysis presented in subsequent sections.

## VII. INTERPLAY OF STRAIN MODES AND OCTAHEDRAL ROTATIONS

In this section we explore why the octahedral rotation amplitudes are smaller in  $A2_1am$  compared to those in the single-rotation structures. As we will show, this provides the key to understanding the pressure response of  $A2_1am$ .

We first observe that the  $X_3^-$  and  $X_2^+$  octahedral rotations couple to “competing” strain states. To make this point clear, we compute the strain of the fully relaxed single-rotation structures ( $Acam$  and  $Amam$ ) as well as  $A2_1am$  with respect to the relaxed  $I4/mmm$  structure. Taking the example of  $Ca_3Ti_2O_7$ , for  $Acam$  we find  $(\eta_{xx}, \eta_z, \eta_o) = (-0.025, 0.025, 0.00)$ , meaning that the cell is compressed in the  $ab$  plane and elongated along  $c$  (this is expected because the  $X_2^+$  rotation bends the  $B-O-B$  angles in the  $ab$  plane). In contrast, for  $Amam$   $(\eta_{xx}, \eta_z, \eta_o) = (0.004, -0.014, 0.011)$ , so the cell is slightly expanded in the  $ab$  plane and compressed along  $c$ . The opposite signs of the strain in these two single-rotation structures indicate that, when both rotations are present (as in  $A2_1am$ ), the strain state (unit cell shape) must be a compromise between the two single-rotation strain states. The result is that the strain in  $A2_1am$  is an order of magnitude smaller than in the single-rotation structures:  $(\eta_{xx}, \eta_z, \eta_o) = (0.002, -0.005, -0.007)$ . The strains in  $Sr_3Zr_2O_7$  and  $Sr_3Sn_2O_7$  are similar, and are reported in Appendix D.

This observation is significant because the reduction of the strain amplitudes in  $A2_1am$  also suppresses the octahedral rotation amplitudes. This is because the amplitudes are partially determined by the strain coupling term, as is clear from Eq. (3). This also can be seen by performing the following computational experiment: we start by computing (for example) the  $X_2^+$  octahedral rotation amplitude in the fully relaxed single-rotation  $Acam$  structure. We then compare this to the  $X_2^+$  amplitude obtained from a structural relaxation of  $Acam$ , where only the atomic positions are allowed to vary and the lattice parameters are fixed at their  $I4/mmm$  values. The difference in  $X_2^+$  amplitude between these two calculations reveals the contribution of the strain term. Finally, we find the

TABLE II. Amplitudes of the  $X_3^-$  and  $X_2^+$  octahedral rotations for structures that are fully relaxed (lattice parameters and atomic positions) and those where the lattice parameters are fixed at their  $I4/mmm$  values and the atomic positions are relaxed. The amplitudes are given in units of Å and are for a 48-atom cell. The rotation amplitudes of the fully relaxed  $A2_1am$  structure are given in Table I, and are similar to those presented here because the  $I4/mmm$  and  $A2_1am$  relaxed lattice parameters are almost the same.

Irrep	Structure	$Sr_3Zr_2O_7$	$Ca_3Ti_2O_7$	$Sr_3Sn_2O_7$
$X_2^+$	$Acam$ (fully relaxed)	1.84	1.71	1.62
	$Acam$ (atoms only)	1.49	1.48	1.32
	$A2_1am$ (atoms only)	1.18	1.23	1.08
$X_3^-$	$Amam$ (fully relaxed)	2.01	1.84	1.82
	$Amam$ (atoms only)	1.96	1.79	1.77
	$A2_1am$ (atoms only)	1.80	1.67	1.67

$X_2^+$  amplitude in  $A2_1am$  where again the atomic positions are optimized but the lattice parameters are fixed to their  $I4/mmm$  values. This second comparison reveals the effect of the terms that couple the structural order parameters in Eq. (4). Table II presents the results of these calculations.

Taking the example of  $Sr_3Zr_2O_7$  in Table II, we find that constraining the lattice parameters to their  $I4/mmm$  values (eliminating strain coupling) significantly reduces  $Q_R$ , from 1.84 to 1.49 Å, that is  $\Delta Q_{R1} = 0.35$  Å. Then, the inclusion of the coupling terms in Eq. (4) ( $A2_1am$ ) reduces the amplitude to 1.18 Å, which results in  $\Delta Q_{R2} = 0.31$  Å. Thus these two mechanisms suppress  $Q_R$  by about the same amount and the total suppression is  $\Delta Q_R = 0.66$  Å.  $Sr_3Sn_2O_7$  and  $Ca_3Ti_2O_7$  exhibit a similar trend (Table II). For the  $X_3^-$  rotation, again both mechanisms contribute to suppressing  $Q_T$ , but the role of the strain coupling is less important. Again using the example of  $Sr_3Zr_2O_7$ , Table II shows that constraining the lattice parameters to their  $I4/mmm$  values suppresses  $Q_T$  from 2.01 to 1.96 Å ( $\Delta Q_{T1} = 0.05$  Å) and including the Eq. (4) coupling terms suppresses it to 1.80 Å ( $\Delta Q_{T2} = 0.16$  Å). In this case, the total suppression is  $\Delta Q_T = 0.21$  Å, significantly smaller than the suppression of  $Q_R$ .

Thus the suppression of the octahedral rotation amplitudes in  $A2_1am$  arises from the combined effect of the suppressed strain terms as well as the presence of couplings to the other distortions. Significantly, this mechanism also is present at finite pressures, thereby reducing the distortion amplitudes and their rate of change with pressure.

## VIII. PRESSURE DEPENDENCE OF LANDAU COEFFICIENTS

The analysis in the previous section has shown that the small strains present in  $A2_1am$  suppress the octahedral rotation amplitudes. However, this mechanism is present in all our materials: so what leads to the differences between materials seen in Fig. 4? The difference can be found by exploring how the Landau coefficients in Eq. (4) vary with pressure in the different materials.

We compute the pressure dependence of the coefficients by fitting Eq. (4) to energy surfaces computed with DFT at a series of pressures ranging from 0 to 18 GPa, as described in

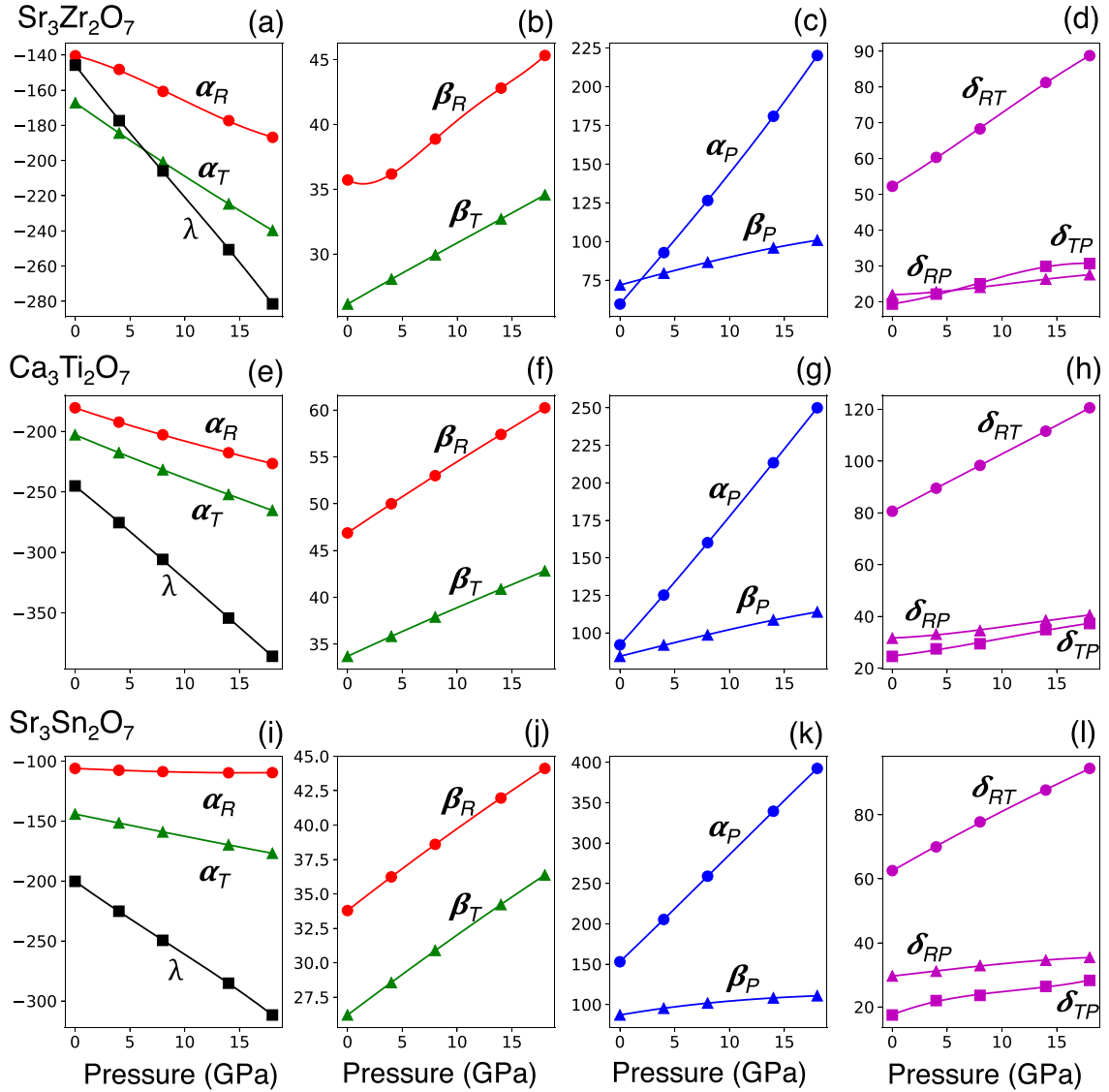


FIG. 5. Pressure dependence of the Landau coefficients given in Eq. (4) for (a)–(d)  $\text{Sr}_3\text{Zr}_2\text{O}_7$ , (e)–(h)  $\text{Ca}_3\text{Ti}_2\text{O}_7$ , and (i)–(l)  $\text{Sr}_3\text{Sn}_2\text{O}_7$ . The units of the second order ( $\alpha_i$ ), fourth order ( $\beta_i, \delta_{ij}$ ), and trilinear ( $\lambda$ ) coefficients are  $(\text{meV}/\text{f.u.}/\text{\AA}^2)$ ,  $(\text{meV}/\text{f.u.}/\text{\AA}^4)$ , and  $(\text{meV}/\text{f.u.}/\text{\AA}^3)$ , respectively.

Appendix E. The energy surface calculations are performed with the lattice parameters fixed to their  $I4/mmm$  values, relaxed at each pressure. Due to the role of strain coupling in determining the octahedral rotation amplitudes, this choice has a significant effect, which we discuss more below.

Figure 5 presents the pressure dependence of the coefficients in Eq. (4) computed for  $\text{Sr}_3\text{Zr}_2\text{O}_7$ ,  $\text{Ca}_3\text{Ti}_2\text{O}_7$ , and  $\text{Sr}_3\text{Sn}_2\text{O}_7$ . For all three compounds, the second order coefficients  $\alpha_R$  and  $\alpha_T$  are negative, indicating that  $I4/mmm$  is unstable with respect to the  $X_3^-$  and  $X_2^+$  octahedral rotations [Figs. 5(a), 5(e), and 5(i)]. These coefficients become more negative with pressure, although the amount of change with pressure varies between the materials. For example, going from 0 to 18 GPa,  $\alpha_R$  changes by about 4  $\text{meV}/\text{f.u.}/\text{\AA}^2$  in  $\text{Sr}_3\text{Sn}_2\text{O}_7$ , whereas for  $\text{Sr}_3\text{Zr}_2\text{O}_7$  and  $\text{Ca}_3\text{Ti}_2\text{O}_7$  it changes by about 45  $\text{meV}/\text{f.u.}/\text{\AA}^2$ . The trilinear coupling coefficient  $\lambda$  is also large and negative, and its amplitude increases signifi-

cantly (130–150  $\text{meV}/\text{f.u.}/\text{\AA}^3$  going from 0 to 18 GPa) in all three materials.

As shown in Figs. 5(b), 5(f), and 5(j), the fourth order coefficients  $\beta_R$  and  $\beta_T$  are positive and increase with pressure. From Eq. (3), it is clear that there is a competition between  $\alpha_T$  and  $\beta_T$  in determining the pressure response of  $Q_T$ : increasing  $|\alpha_T|$  leads to a larger rotation amplitude, whereas increasing  $\beta_T$  suppresses the rotation. Contrasting with the quadratic coefficients, the pressure evolution of  $\beta_R$  and  $\beta_T$  is fairly similar for all three materials.

In all three materials,  $I4/mmm$  is stable with respect to the polar distortion, so  $\alpha_P$  and  $\beta_P$  are positive [Figs. 5(c), 5(g), and 5(k)]. The second order coefficient  $\alpha_P$  increases significantly with pressure, whereas  $\beta_P$  increases more gradually. Interestingly, we find that  $\alpha_P$  increases the most in  $\text{Sr}_3\text{Sn}_2\text{O}_7$ , which contrasts with  $\alpha_R$  and  $\alpha_T$  which changed the least under pressure compared to the other materials. Finally, Figs. 5(d),

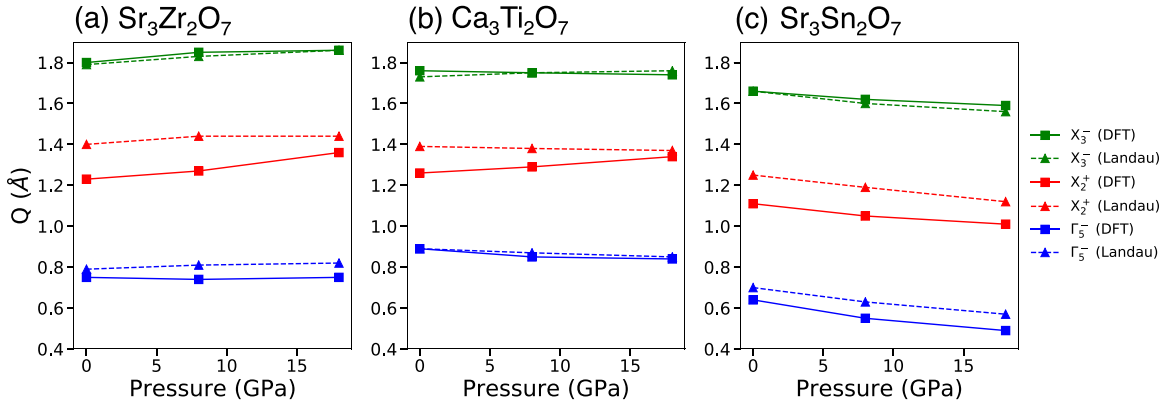


FIG. 6. Comparison of  $A2_1am$  distortion amplitudes computed from DFT (solid lines) and from a Landau expansion that neglects all coupling terms (dashed lines) for (a)  $\text{Sr}_3\text{Zr}_2\text{O}_7$ , (b)  $\text{Ca}_3\text{Ti}_2\text{O}_7$ , and (c)  $\text{Sr}_3\text{Sn}_2\text{O}_7$ . The  $X_3^-$  and  $X_2^+$  amplitudes from the Landau theory are obtained by minimizing Eq. (1). The  $\Gamma_5^-$  Landau theory amplitude is obtained by minimizing Eq. (4) with respect to  $Q_P$ , with  $Q_T$  and  $Q_R$  fixed to the values obtained by minimizing Eq. (1).

5(h), and 5(l) show the pressure evolution of the biquadratic coupling coefficients  $\delta_{RT}$ ,  $\delta_{RP}$ , and  $\delta_{TP}$ . These coefficients are all positive and increase with pressure. For all three compounds,  $\delta_{RT}$  is the largest and has the most significant change with pressure (about 40 meV/f.u./ $\text{\AA}^4$  going from 0 to 18 GPa), whereas  $\delta_{RP}$  and  $\delta_{TP}$  only increase slightly under pressure.

Armed with this analysis, we revisit the origin of the different pressure responses shown in Fig. 4. As discussed above, the coefficients change under pressure by about the same amount in all three compounds, with the exception of the quadratic coefficients  $\alpha_R$ ,  $\alpha_T$ , and  $\alpha_P$ . We can understand that the origin of the decreasing octahedral rotation amplitude under pressure in  $\text{Sr}_3\text{Sn}_2\text{O}_7$  simply comes from the very weak pressure dependence of  $\alpha_R$ , while  $\beta_R$  still strongly increases with pressure. We can rationalize the differences in the evolution of  $Q_T$  under pressure in the same way. From Fig. 5, it is clear that the change in  $\alpha_T$  is the largest for  $\text{Sr}_3\text{Zr}_2\text{O}_7$ , somewhat smaller for  $\text{Ca}_3\text{Ti}_2\text{O}_7$ , and the smallest for  $\text{Sr}_3\text{Sn}_2\text{O}_7$ . This results in  $Q_T$  increasing with pressure for  $\text{Sr}_3\text{Zr}_2\text{O}_7$ , almost not changing for  $\text{Ca}_3\text{Ti}_2\text{O}_7$ , and decreasing for  $\text{Sr}_3\text{Sn}_2\text{O}_7$ .

The polar distortion amplitude  $Q_P$  arises from the interplay of the trilinear coupling coefficient  $\lambda$  and the quadratic coefficient  $\alpha_P$ . The coefficient  $\lambda$  becomes much more negative with pressure which on its own would increase  $Q_P$ ; however, the substantial increase in  $\alpha_P$  counteracts this and leads to the slight decrease in  $Q_P$  with pressure as shown in Fig. 4(c). The amplitude  $Q_P$  decreases most strongly with pressure in  $\text{Sr}_3\text{Sn}_2\text{O}_7$ , because for this material  $\alpha_P$  increases the most under pressure. At the microscopic level, the differences between  $\alpha_R$ ,  $\alpha_T$ , and  $\alpha_P$  in the different materials are likely due to a combination of tolerance factor,  $B$ -site chemistry, and bonding preferences. We present a complementary analysis in Appendix F, where we analyze the pressure dependence of the individual energy terms in Eq. (4), which also leads to the same picture.

Finally, in order to assess the quality of our Landau expansion, Fig. 6 shows a comparison of the  $A2_1am$  distortion amplitudes computed from DFT (reproduced from Fig. 4), and the amplitudes that minimize the Landau energy. The  $X_3^-$

and  $X_2^+$  rotation amplitudes ( $Q_T$  and  $Q_R$ , respectively) shown in Fig. 6 are obtained by minimizing Eq. (1), whereas the  $\Gamma_5^-$  amplitude ( $Q_P$ ) is obtained by minimizing Eq. (4) with respect to  $Q_P$  [with  $Q_T$  and  $Q_R$  fixed to the values obtained by the minimization of Eq. (1)]. Interestingly, we find that the Landau results reproduce the DFT results, despite the fact that we have neglected the coupling terms for the  $X_3^-$  and  $X_2^+$  rotations. This is because the Landau coefficients were calculated with fixed  $I4/mmm$  lattice parameters (strain set to zero). The difference in amplitude of the  $X_2^+$  rotation is due to the neglect of the coupling terms, although the rate of change with pressure is well captured. For the case of the  $X_3^-$  rotations, the DFT and Landau amplitudes match almost exactly (this is somewhat an artifact, which we discuss further in Appendix E), as does the slope. An important conclusion of this analysis is that the pressure dependence of the octahedral rotation amplitudes in the polar  $A2_1am$  structure are well reproduced by just considering the single rotation phases (and preventing the strain relaxation by constraining the lattice parameters to their  $I4/mmm$  values).

## IX. DISCUSSION

To summarize, in this work we explore how octahedral rotations in hybrid improper ferroelectric  $\text{Sr}_3\text{Zr}_2\text{O}_7$ ,  $\text{Ca}_3\text{Ti}_2\text{O}_7$ , and  $\text{Sr}_3\text{Sn}_2\text{O}_7$  (and related  $A$ -site substituted compounds) respond to pressure. When constrained to structures that are distorted by a single octahedral rotation, the pressure response of these materials is largely in line with expectations from the  $A/B$ -site formal charge descriptor developed for  $\text{ABO}_3$  perovskites (that is, the rotation amplitudes increase with pressure). We find some exceptions, for example,  $\text{Sr}_3\text{Sn}_2\text{O}_7$  when constrained to space groups  $Amam$  and  $P4_2/nmn$  ( $a^-a^-c^0$  rotations), which we attribute to a combination of the tolerance factor,  $B$ -site chemistry, and competing bonding preferences in the RP structure. We find a more complex pressure response for the polar  $A2_1am$  structures:  $\text{Sr}_3\text{Zr}_2\text{O}_7$  is in line with the formal charge descriptor, whereas  $\text{Sr}_3\text{Sn}_2\text{O}_7$  and  $\text{Ca}_3\text{Ti}_2\text{O}_7$  behave differently.

We find that the origin of the diverse pressure behavior of the  $A2_1am$  structures is the suppression of the octahedral



rotation amplitudes compared to their values in single-rotation structures. This occurs due to the combined effect of reduced strain and couplings between structural order parameters. The strain is suppressed in  $A2_1am$  because the  $X_3^-$  and  $X_2^+$  rotations are stabilized by strains of opposite sign (e.g., contraction/expansion along  $c$ ). The result is that subtle differences between the materials (tied to tolerance factor,  $B$ -site chemistry, and bonding) can then lead to qualitatively different octahedral rotation responses to pressure (increasing vs decreasing). These differences also are evident from the pressure dependence of the coefficients of a Landau free energy expansion. We note that unravelling differences in chemical bonding between the materials as well as the precise role of bonding in determining octahedral rotation amplitudes may require a level of theory beyond the PBEsol functional. This would be an interesting topic for a future study.

We also find that the pressure evolution of the  $A2_1am$  structure can be predicted from the pressure response of single-rotation structures, with the lattice parameters held to their  $I4/mmm$  values (which nearly zeroes the strain coupling terms). This provides a simple rule for predicting pressure evolution, which may generalize to other RP compounds.

Furthermore, we expect the findings presented here to be relevant for understanding how other “knobs” for manipulating crystal structure such as chemical substitution and epitaxial strain influence octahedral rotations in RPs. Although the structural response to pressure may not directly correspond to the structural changes induced by these other knobs, the factors that influence the response will generally be similar. This could facilitate the identification of strategies to manipulate polarization for use in thin film based memory and storage technologies.

Finally, we note that in this work we have focused our analysis on the pressure evolution of octahedral rotation amplitudes within crystal structures of given symmetries. Alternatively, the application of pressure can lead to a phase transition to a different symmetry structure. In a recent paper [52] with our experimental collaborators, we have shown that  $\text{Sr}_3\text{Sn}_2\text{O}_7$  undergoes a pressure-driven sequence of structural phase transitions at room temperature  $A2_1am \rightarrow Pnab \rightarrow Acaa \rightarrow I4/mmm$ . These transitions occur at 2, 15, and 18 GPa, respectively. Here the  $Pnab$  structure has an  $a^-a^-c^-$  octahedral rotation pattern and  $Acaa$  has  $a^0a^0c^-$  rotations. To explore the possibility of structural phase transitions in  $\text{Ca}_3\text{Ti}_2\text{O}_7$  and  $\text{Sr}_3\text{Zr}_2\text{O}_7$ , Appendix H shows DFT calculations of the enthalpy differences  $\Delta H = \Delta E + P\Delta V$  between possible high pressure phases and the  $A2_1am$  ground state. Our  $T = 0$  calculations for pressures up to 18 GPa show that  $A2_1am$  remains the lowest enthalpy phase. However, at room temperature other phases may become accessible at lower pressures.

The pressure response revealed in the  $n = 2$  RPs in this work highlights both their structural complexity and their tunability. Looking forward, expanding this study to include  $n = 2$  RPs with partially filled  $d$  orbitals (e.g.,  $\text{Ca}_3\text{Mn}_2\text{O}_7$ ) and with different formal charge states (e.g.,  $\text{CaTb}_2\text{Fe}_2\text{O}_7$ ) would enable further understanding of the pressure response. Furthermore, investigating RPs with different values of  $n$  could provide additional insight into the role of dimensionality and

competing bonding preferences in these materials. The  $n = 1$  RPs would be of particular interest in this context, because the layering of single perovskite and rocksalt layers would create a different balance of  $A$ -site bonding preferences. Finally, the pressure dependence of octahedral rotations in other layered perovskite families, such as the Aurivillius and Dion-Jacobson phases, is another open area for future exploration. Taken together, the results presented in this work advance our understanding of the behavior of  $n = 2$  RPs under compression, and provide a framework for future studies of related materials.

## ACKNOWLEDGMENTS

This research used resources of the Center for Functional Nanomaterials, which is a U.S. DOE Office of Science Facility, and the Scientific Data and Computing Center, a component of the Computational Science Initiative, at Brookhaven National Laboratory under Contract No. DE-SC0012704. This work also used the Extreme Science and Engineering Discovery Environment (XSEDE) Comet Cluster at the San Diego Supercomputer Center through the HPC@UC program. In addition, we acknowledge the use of computational resources supported by Academic and Research Computing Systems at the New Jersey Institute of Technology. The authors would like to acknowledge useful discussions with K. Rabe and D. Vanderbilt, as well as C. S. Hellberg, P. Nukala, and R. Cohen during the Ferro-2020 workshop.

## APPENDIX A: SINGLE ROTATION RP STRUCTURAL PHASES

In this Appendix we present the details of the single-rotation RP phases that we explore in Sec. IV of the main text. Table III presents the lattice parameters, octahedral rotation amplitudes, and energies (with respect to the  $A2_1am$  ground state) of the single-rotation phases computed at 0 GPa.

Figure 7 presents the pressure evolution of the  $X_3^-$  octahedral rotation amplitude ( $Q_T$ ) in the  $P4_2/mnm$  structure for a series of  $A_P(A_{RS})_2B_2O_7$  compounds ( $B = \text{Zr, Ti, Sn}$ ). With the exception of  $\text{Sr}_3\text{Sn}_2\text{O}_7$  and  $\text{BaSr}_2\text{Sn}_2\text{O}_7$ , the  $X_3^-$  amplitude increases with pressure for all other compounds. The slopes  $dQ_T/dP$  reported in Fig. 3 of the main text are obtained by fitting the data in Fig. 7.

## APPENDIX B: PRESSURE DEPENDENCE OF OCTAHEDRAL ROTATIONS IN $ABO_3$ PEROVSKITE OXIDES

This Appendix presents the evolution of the octahedral rotation amplitudes with pressure for the perovskites  $\text{SrZrO}_3$ ,  $\text{CaTiO}_3$ , and  $\text{SrSnO}_3$  to facilitate comparison with the analogous RP phases presented in the main text. Figure 8 shows the pressure dependence of the single-rotation phases  $Imma$  ( $a^-a^-c^0$  octahedral rotations, transforming like the  $R_5^-$  irrep of the high-symmetry reference structure  $Pm\bar{3}m$ ) and  $P4/mbm$  ( $a^0a^0c^+$  octahedral rotations, transforming like  $M_2^+$ ). In both structural phases, and for all three compounds, we find that the octahedral rotation amplitudes increase with pressure.

Figure 9 shows the pressure evolution of the same set of perovskites in their ground state  $Pbnm$  phase. The octahedral

TABLE III. Lattice parameters, octahedral rotation amplitudes (in Å), and energies (in meV/f.u.) of the high-symmetry reference structure  $I4/mmm$  and the single-rotation structural phases that we consider in the main text computed at 0 GPa. The amplitudes are obtained by decomposing the distorted structure with respect to  $I4/mmm$ , and are reported for a 48 atom cell. The energies are given with respect to the  $A2_1am$  ground state energy, which is set to 0 meV/f.u.

		Sr <sub>3</sub> Zr <sub>2</sub> O <sub>7</sub>	Ca <sub>3</sub> Ti <sub>2</sub> O <sub>7</sub>	Sr <sub>3</sub> Sn <sub>2</sub> O <sub>7</sub>
<i>Acaa</i>	<i>a</i>	5.727	5.324	5.676
	<i>b</i>	5.727	5.323	5.675
	<i>c</i>	21.322	19.868	21.080
	$X_1^-$	1.880	1.780	1.680
	$\Delta E$	119.469	170.810	90.140
<i>Acam</i>	<i>a</i>	5.730	5.325	5.679
	<i>b</i>	5.730	5.325	5.679
	<i>c</i>	21.326	19.876	21.073
	$X_2^+$	1.840	1.750	1.620
	$\Delta E$	155.960	203.050	125.380
<i>Amam</i>	<i>a</i>	5.876	5.479	5.817
	<i>b</i>	5.784	5.394	5.719
	<i>c</i>	20.622	19.106	20.450
	$X_3^-$	2.000	1.890	1.820
	$\Delta E$	62.840	126.490	40.490
<i>P4<sub>2</sub>/mmm</i>	<i>a</i>	5.848	5.451	5.784
	<i>b</i>	5.848	5.451	5.784
	<i>c</i>	20.504	19.009	20.340
	$X_3^-$	2.020	1.910	1.800
	$\Delta E$	42.220	105.730	39.920
<i>I4/mmm</i>	<i>a</i>	4.124	3.835	4.067
	<i>b</i>	4.124	3.835	4.067
	<i>c</i>	20.846	19.382	20.598
	$\Delta E$	394.750	499.036	277.850

rotation pattern in  $Pbnm$  is  $a^-a^-c^+$ . There is trilinear coupling between the  $R_5^-$  and  $M_2^+$  octahedral rotation order parameters and a distortion primarily consisting of antipolar displacements of the A-site cations, which transforms like

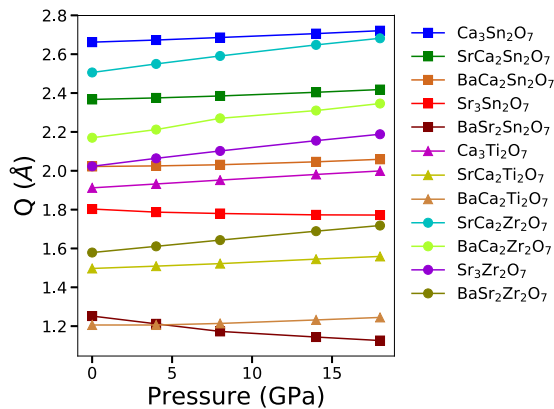


FIG. 7. Amplitude of the  $X_3^-$  octahedral rotation ( $Q$ ) for a series of  $A_P(A_{RS})_2B_2O_7$  compounds ( $B = \text{Zr, Ti, Sn}$ ) in the  $P4_2/mmm$  structure as a function of pressure. For compounds with mixed A sites, the larger cation is placed in the  $A_P$  position, as described in the main text. The amplitudes are reported for a 48 atom cell

$X_5^-$ . The octahedral rotation amplitudes in all three compounds increase with pressure, and the  $X_5^-$  amplitude slightly increases in  $\text{SrZrO}_3$  and  $\text{CaTiO}_3$  and slightly decreases in  $\text{SrSnO}_3$ .

### APPENDIX C: PRESSURE RESPONSE OF ADDITIONAL $A2_1am$ COMPOUNDS

Figure 10 shows the derivatives of the  $X_3^-$  octahedral rotation amplitude ( $dQ_T/dP$ ) and the  $X_2^+$  octahedral rotation amplitude ( $dQ_R/dP$ ) with respect to pressure, computed for a set of  $A_P(A_{RS})_2B_2O_7$  compounds with symmetry  $A2_1am$ . These derivatives were computed by fitting distortion amplitude ( $Q$ ) versus pressure curves, using the same methodology as described in Appendix A. Whereas  $dQ_T/dP$  generally becomes more positive as the tolerance factor decreases, we observe no clear trend in  $dQ_R/dP$  with tolerance factor.

### APPENDIX D: STRAIN MODES

Table IV shows the amplitudes of the three active strain modes in the RP phases that we consider in the main text.

### APPENDIX E: LANDAU FREE ENERGY EXPANSION

This Appendix describes our method for finding the pressure-dependent coefficients of the Landau expansion presented in Eq. (4) in the main text. Figure 11 presents an example of the energy surfaces we use in this analysis. For each pressure at which we compute the Landau coefficients, we start by performing DFT structural relaxations of the high-symmetry  $I4/mmm$  structure at that pressure. Then, keeping the lattice parameters fixed at the  $I4/mmm$ -relaxed values for a given pressure, we freeze in several distortion amplitudes and then use DFT to compute the total energy of each “frozen” structure to generate an energy surface. By fitting this energy surface we obtain the coefficients at a given pressure.

We obtain the second- and fourth-order coefficients  $\alpha_i$  and  $\beta_i$  by freezing in a single distortion and fitting the resulting energy surface as shown in Figs. 11(a) and 11(b). To obtain the biquadratic coupling coefficients  $\delta_{RT}$ ,  $\delta_{RP}$ , and  $\delta_{TP}$ , we condense a fixed amplitude of one distortion, and then freeze in the second distortion. For example, to find  $\delta_{RT}$  we fix the  $X_2^+$  rotation amplitude to  $Q_{R0} = 0.2$  Å, and then freeze in increasing amplitudes of  $Q_T$ , as shown in Fig. 11(d). We then extract  $\delta_{RT}$  by fitting to the function

$$f(Q_{R0}, Q_T) = \alpha_T Q_T^2 + \beta_T Q_T^4 + \delta_{RT} Q_{R0}^2 Q_T^2, \quad (\text{E1})$$

where the coefficients  $\alpha_T$  and  $\beta_T$  are fixed to the values obtained from Fig. 11(a), as described above. The coefficients  $\delta_{RP}$  and  $\delta_{TP}$  are found in an analogous manner [Figs. 11(e) and 11(f)]. We obtain the trilinear coupling coefficient  $\lambda$  by setting the octahedral rotation amplitudes to fixed values  $Q_{R0}$  and  $Q_{T0}$ , and freezing in increasing amplitudes of  $Q_P$ . We extract  $\lambda$  by fitting to the function

$$f(Q_{R0}, Q_{T0}, Q_P) = \lambda Q_{R0} Q_{T0} Q_P + \alpha_P Q_P^2 + \beta_P Q_P^4 + \delta_{RP} Q_{R0}^2 Q_P^2 + \delta_{TP} Q_{T0}^2 Q_P^2, \quad (\text{E2})$$

where the  $\alpha_i$  and  $\delta_{ij}$  coefficients are fixed to the values obtained as described above. All coefficients computed at a

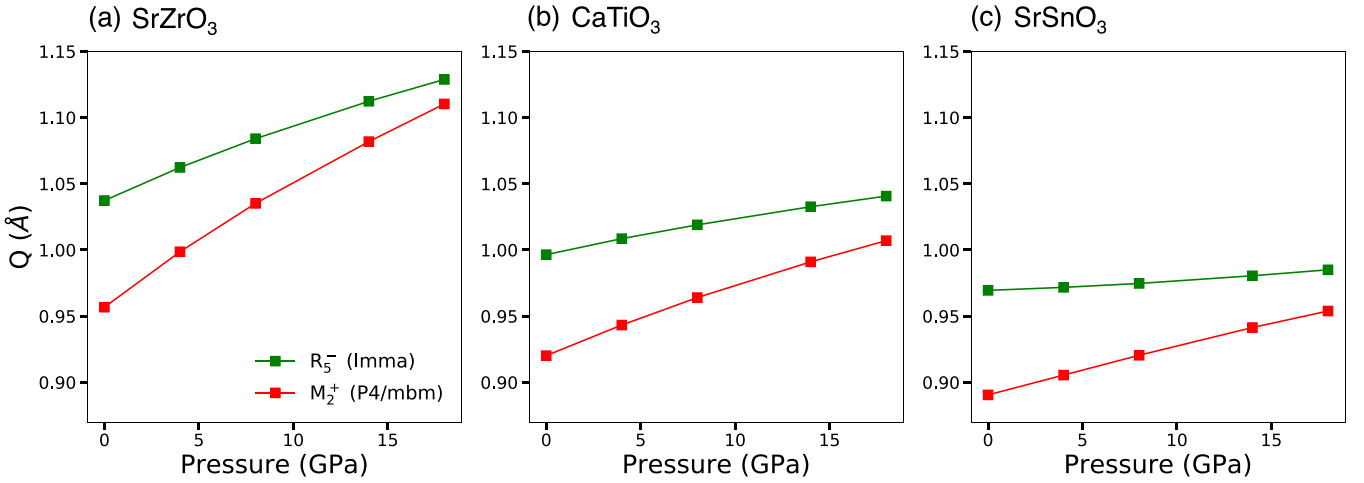


FIG. 8. Pressure dependence of octahedral rotation amplitudes ( $Q$ ) for (a)  $\text{SrZrO}_3$ , (b)  $\text{CaTiO}_3$ , and (c)  $\text{SrSnO}_3$  in single octahedral rotation structural phases:  $Imma$  ( $a^- a^- c^0$  rotations transforming like  $R_5^-$ ) and  $P4/mbm$  ( $a^0 a^0 c^+$  rotations transforming like  $M_2^+$ ). The octahedral rotation amplitudes are reported in Å for a 20 atom unit cell.

series of pressures ranging from 0 to 18 GPa for  $\text{Sr}_3\text{Zr}_2\text{O}_7$ ,  $\text{Ca}_3\text{Ti}_2\text{O}_7$ , and  $\text{Sr}_3\text{Sn}_2\text{O}_7$  are reported in Table V.

A subtlety that arises in the computation of the energy surfaces is the choice of the relative amplitudes of the different atomic displacements that contribute to a given distortion. Although the  $X_2^+$  distortion consists solely of planar oxygen displacements, the  $X_3^-$  and  $\Gamma_5^-$  distortions are built from a combination of  $A$ -site,  $B$ -site, apical oxygen, and planar oxygen displacements. The relative amplitudes of these displacements can vary, while still maintaining the same symmetry. Thus, when freezing in these displacements, a choice about their relative amplitudes must be made. Here, for each pressure we obtain the relative amplitudes by decomposing the fully DFT-relaxed (lattice parameters and atomic positions)  $A2_1am$  structure with respect to  $I4/mmm$ .

To make this statement more precise, we let  $\mathbf{R}_{I4/mmm}$  and  $\mathbf{R}_{A2_1am}$  be vectors containing the atomic positions of the

$I4/mmm$  and  $A2_1am$  structures, respectively. We can then write

$$\mathbf{R}_{A2_1am} = \mathbf{R}_{I4/mmm} + \mathbf{u}, \quad (\text{E3})$$

where  $\mathbf{u}$  is a vector that contains the atomic displacements away from their high-symmetry positions. The vector  $\mathbf{u}$  can then be decomposed into distortions that transform like irreps of  $I4/mmm$ :

$$\mathbf{u} = \sum_{j=1}^4 A_{j\Gamma_1^+} \mathbf{u}_{j\Gamma_1^+} + \sum_{j=1}^6 A_{jX_3^-} \mathbf{u}_{jX_3^-} + \sum_{j=1}^2 A_{jX_2^+} \mathbf{u}_{jX_2^+} + \sum_{j=1}^7 A_{j\Gamma_5^-} \mathbf{u}_{j\Gamma_5^-}, \quad (\text{E4})$$

where  $\mathbf{u}_{j\sigma}$  is the normalized symmetry adapted mode that transforms like irrep  $\sigma$  ( $\sigma = \Gamma_1^+, X_3^-, X_2^+, \Gamma_5^-$ ) of  $I4/mmm$ .

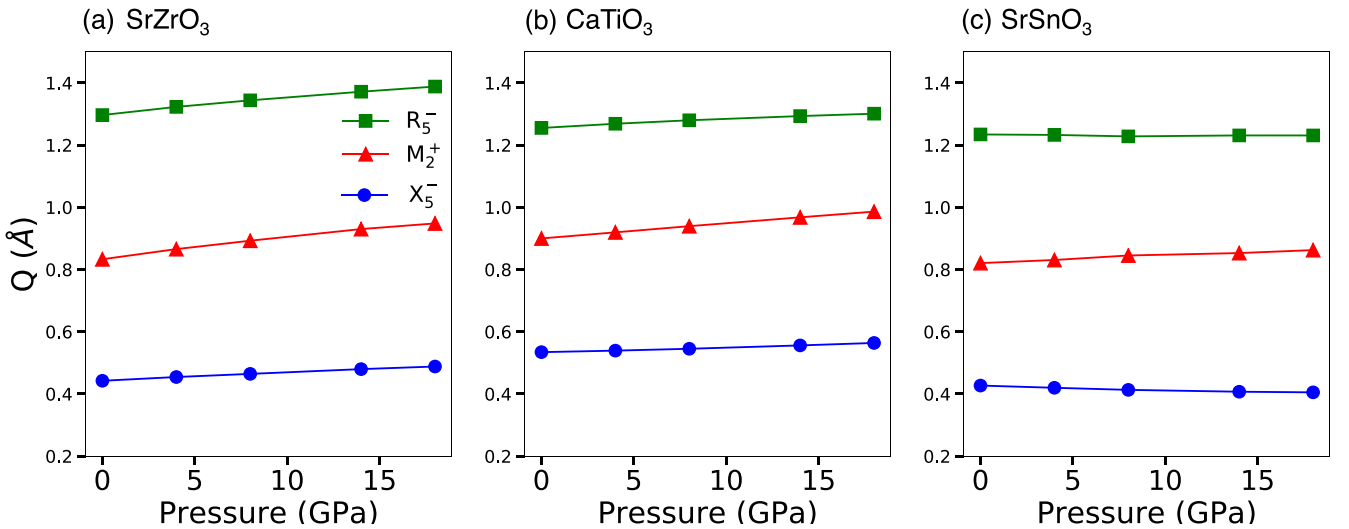


FIG. 9. Pressure dependence of the octahedral rotation amplitudes ( $Q$ ) that contribute to the ground state  $Pbnm$  structure of (a)  $\text{SrZrO}_3$ , (b)  $\text{CaTiO}_3$ , and (c)  $\text{SrSnO}_3$ . For each material, the amplitudes of the  $R_5^-$ ,  $M_2^+$ , and  $X_5^-$  distortions are shown. The distortion amplitudes are reported in Å for a 20 atom unit cell.

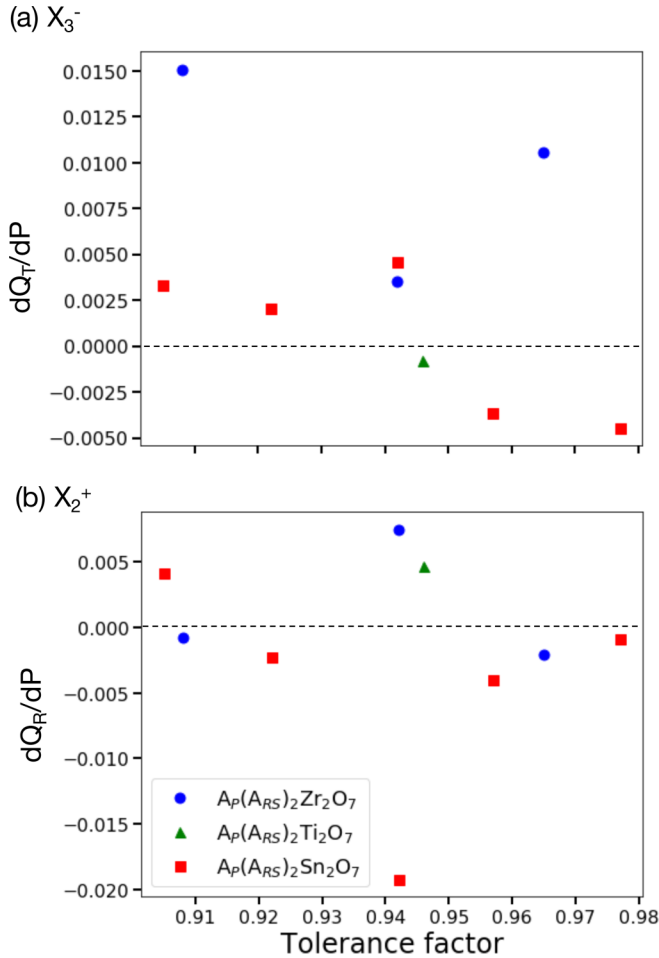


FIG. 10. Derivative of (a) the  $X_3^-$  rotation amplitude ( $Q_T$ ) and (b) the  $X_2^+$  rotation amplitude ( $Q_R$ ) with respect to pressure for a family of  $A_P(A_{RS})_2B_2O_7$  compounds, plotted versus tolerance factor. For  $B = \text{Zr}$ , the compounds considered (in order of decreasing tolerance factor) are  $\text{BaSr}_2\text{Zr}_2\text{O}_7$ ,  $\text{Sr}_3\text{Zr}_2\text{O}_7$ , and  $\text{SrCa}_2\text{Zr}_2\text{O}_7$ . For  $B = \text{Sn}$ , the compounds shown are  $\text{BaSr}_2\text{Sn}_2\text{O}_7$ ,  $\text{BaCa}_2\text{Sn}_2\text{O}_7$ ,  $\text{Sr}_3\text{Sn}_2\text{O}_7$ ,  $\text{SrCa}_2\text{Sn}_2\text{O}_7$ , and  $\text{Ca}_3\text{Sn}_2\text{O}_7$  in order of decreasing tolerance factor.

TABLE IV. Strain mode amplitudes obtained by decomposing the DFT-relaxed distorted phases in the left column with respect to the  $I4/mmm$  reference structure. The strains  $\eta_{xx}$ ,  $\eta_z$ , and  $\eta_o$  are uniform expansion in the  $ab$  plane, expansion along  $c$ , and the orthorhombic distortion, respectively.

Symmetry	Strain	$\text{Sr}_3\text{Zr}_2\text{O}_7$	$\text{Ca}_3\text{Ti}_2\text{O}_7$	$\text{Sr}_3\text{Sn}_2\text{O}_7$
$A_{cam}$	$\eta_{xx}$	-0.025	-0.025	-0.018
	$\eta_z$	0.023	0.025	0.023
	$\eta_o$	0.0	0.0	0.0
$A_{mam}$	$\eta_{xx}$	0.000	0.004	0.004
	$\eta_z$	-0.012	-0.014	-0.007
	$\eta_o$	0.011	0.011	0.012
$A_{21am}$	$\eta_{xx}$	-0.007	-0.002	-0.001
	$\eta_z$	-0.002	-0.005	0.001
	$\eta_o$	-0.001	-0.007	0.002

The  $\Gamma_1^+$  distortions do not alter the symmetry, and we do not discuss them further. The coefficient  $A_{j\sigma} = \mathbf{u} \cdot \mathbf{u}_{j\sigma}$  gives the amplitude that mode  $\mathbf{u}_{j\sigma}$  contributes to the total distortion amplitude  $|\mathbf{u}|$  and is obtained from a decomposition of the DFT-relaxed  $A_{21am}$  structure. The total distortion amplitudes presented throughout this work are computed as  $A_\sigma = \sqrt{\sum_j A_{j\sigma}^2}$ .

We then calculate energy surfaces by building a sequence of structures [taking the example of the  $X_3^-$  energy surface in Fig. 11(a)]

$$\mathbf{R}_{Amam,k} = \mathbf{R}_{I4/mmm} + X_k u_{X_3^-}, \quad (\text{E5})$$

where  $X_k$  takes values 0, 0.1, 0.2, and so on, and

$$u_{X_3^-} = \frac{1}{N_{X_3^-}} \sum_{j=1}^6 A_{jX_3^-} u_{jX_3^-}. \quad (\text{E6})$$

The normalization factor ( $N_{X_3^-}$ ) is given by

$$N_{X_3^-} = \sqrt{\sum_{j=1}^6 A_{jX_3^-}^2}. \quad (\text{E7})$$

## APPENDIX F: PRESSURE DEPENDENCE OF INDIVIDUAL LANDAU ENERGY TERMS

Building on the analysis of the pressure-dependent Landau coefficients presented in the main text, in this Appendix we explore the pressure dependence of individual energy terms in Eq. (4). Figure 12 shows the energy of each term in Eq. (4) for several pressures. These energies are calculated using the pressure-dependent Landau coefficients from Fig. 5 and the DFT-relaxed amplitudes  $Q_T$ ,  $Q_R$ , and  $Q_P$ . For all three compounds and at all pressures, the largest energy lowering contributions are from the  $\alpha_i Q_i^2$  and trilinear terms, and the largest energy raising contribution is from the biquadratic  $\delta_{TR} Q_T^2 Q_R^2$  term. The biquadratic terms involving  $Q_P$  are negligible in all cases. The data presented in Fig. 12 also is reported in Table VI.

To more clearly see how the energy terms change with pressure, we plot the difference in energy at pressure  $P$  from its value at 0 pressure in Fig. 13. For simplicity, here we group together the quadratic and quartic terms for each distortion, that is,  $E(Q_i) = \alpha_i Q_i^2 + \beta_i Q_i^4$ . The biquadratic terms involving  $Q_P$  are not shown.

For  $\text{Sr}_3\text{Zr}_2\text{O}_7$ ,  $E(Q_R)$ ,  $E(Q_T)$ , and  $\lambda Q_R Q_T Q_P$  all become more negative with increasing pressure, whereas  $\delta_{TR} Q_T^2 Q_R^2$  and  $E(Q_P)$  become more positive. The trilinear and biquadratic coupling terms show the most dramatic energy change with pressure. The behavior of  $\text{Ca}_3\text{Ti}_2\text{O}_7$  is very similar to that of  $\text{Sr}_3\text{Zr}_2\text{O}_7$  [Fig. 13(b)]. The  $E(Q_T)$ , trilinear, and biquadratic terms change slightly less with pressure, underlying the observation that  $Q_T$  is almost unchanged with pressure in the main text.

The evolution of the energy terms with pressure for  $\text{Sr}_3\text{Sn}_2\text{O}_7$  is quite distinct [Fig. 13(c)]. Due to its larger tolerance factor, the absolute energy contributions as well their changes with pressure are much smaller. Most notably,  $E(Q_R)$  actually becomes *less* negative with increasing pressure. The

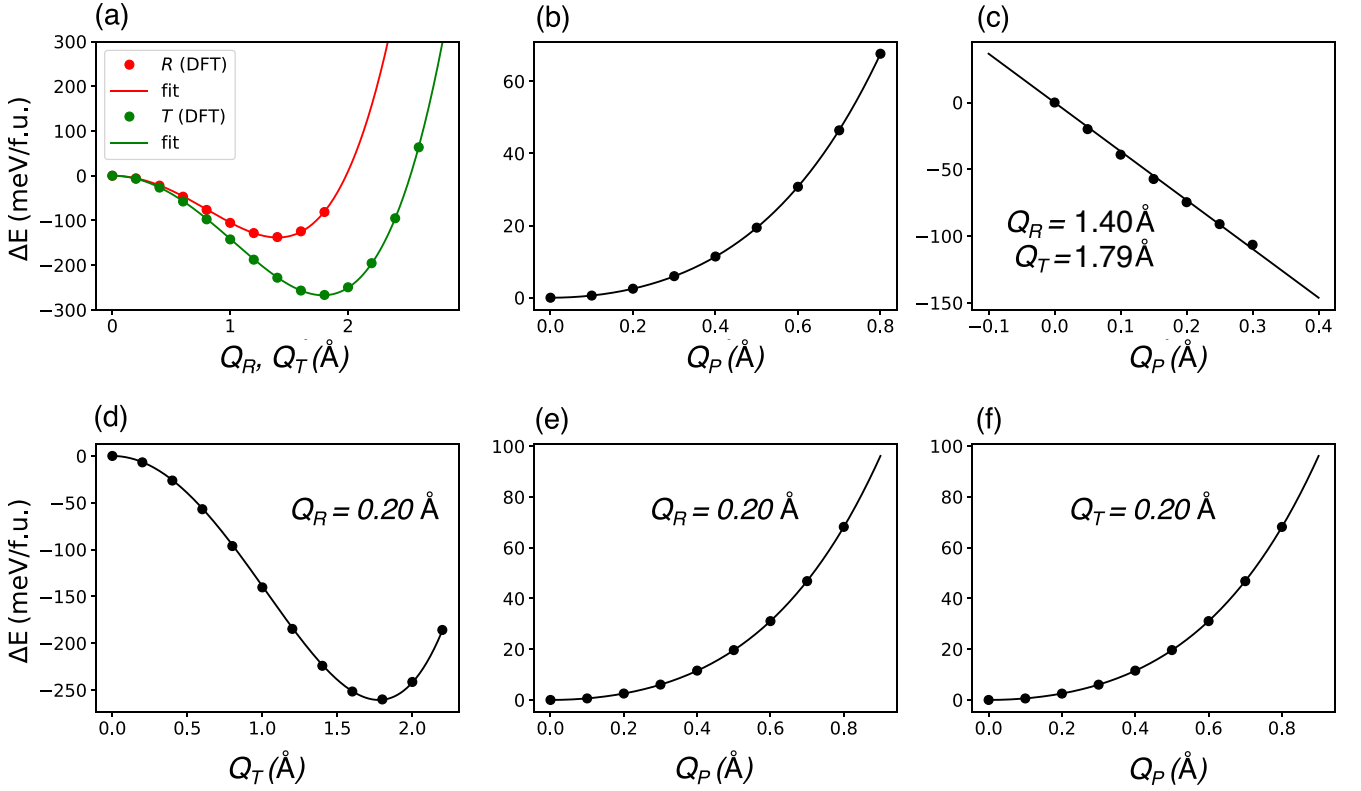


FIG. 11. Energy surfaces used for computing the Landau expansion coefficients for  $\text{Sr}_3\text{Zr}_2\text{O}_7$  at 0 GPa. (a) Energy as a function of  $X_5^-$  rotation amplitude ( $Q_T$ ) and  $X_2^+$  amplitude ( $Q_R$ ). The coefficients  $\alpha_R$ ,  $\beta_R$ ,  $\alpha_T$ , and  $\beta_T$  in Eq. (4) are extracted from fits to these energy surfaces. (b) Energy as a function of the  $\Gamma_5^-$  polar amplitude, which is used to extract  $\alpha_P$  and  $\beta_P$ . (c) Energy as a function of the polar amplitude  $Q_P$  when the octahedral rotations are fixed to  $Q_R = 1.40 \text{ \AA}$  and  $Q_T = 1.79 \text{ \AA}$ , which is used to extract the trilinear coupling coefficient  $\lambda$ . (d) Energy as a function of octahedral rotation amplitude  $Q_T$ , when  $Q_R = 0.2 \text{ \AA}$ , which is used to determine  $\delta_{RT}$ . (e),(f) Energy as a function of  $Q_P$  with either  $Q_R$  or  $Q_T$  fixed to  $0.2 \text{ \AA}$ , which are used to extract  $\delta_{RP}$  and  $\delta_{TP}$ . In all plots, the data points are the DFT results and the lines are the fitted functions.

$E(Q_T)$  and trilinear terms both become more negative with pressure and change by about the same amount, which also contrasts with the other two compounds where the trilinear

term decreases much more rapidly under pressure. Finally,  $E(Q_P)$  and the biquadratic term both become more positive under pressure, but now their rate of change is flipped

TABLE V. Coefficients of the Landau expansion for various pressures for  $\text{Sr}_3\text{Zr}_2\text{O}_7$ ,  $\text{Sr}_3\text{Sn}_2\text{O}_7$ , and  $\text{Ca}_3\text{Ti}_2\text{O}_7$ . The units of second order, fourth order, and trilinear coupling coefficients are (meV/f.u./ $\text{\AA}^2$ ), (meV/f.u./ $\text{\AA}^4$ ), and (meV/f.u./ $\text{\AA}^3$ ), respectively.

	$P$ (GPa)	$\alpha_R$	$\alpha_T$	$\lambda$	$\beta_R$	$\beta_T$	$\alpha_P$	$\beta_P$	$\delta_{RT}$	$\delta_{RP}$	$\delta_{TP}$
$\text{Sr}_3\text{Zr}_2\text{O}_7$	0	-140.46	-167.18	-145.81	35.71	26.15	59.62	71.90	52.24	21.93	19.34
	4	-148.23	-184.47	-177.34	36.18	28.07	92.82	79.52	60.32	22.73	22.13
	8	-160.73	-200.88	-205.91	38.87	29.94	126.47	86.58	68.28	24.01	25.01
	14	-177.32	-224.68	-250.67	42.80	32.71	180.86	95.88	81.24	26.30	29.89
	18	-186.82	-239.74	-281.60	45.32	34.57	220.09	100.83	88.74	27.54	30.67
$\text{Sr}_3\text{Sn}_2\text{O}_7$	0	-106.09	-144.17	-200.25	33.79	26.21	152.97	87.06	62.56	29.66	17.49
	4	-107.62	-151.58	-225.18	36.23	28.56	205.37	95.35	69.96	31.15	21.99
	8	-108.78	-159.11	-249.45	38.60	30.90	258.92	101.83	77.76	32.90	23.62
	14	-109.72	-169.83	-285.21	41.96	34.22	339.37	108.18	87.69	34.59	26.42
	18	-109.59	-176.87	-311.73	44.11	36.38	392.37	110.87	94.45	35.46	28.30
$\text{Ca}_3\text{Ti}_2\text{O}_7$	0	-180.44	-202.78	-245.10	46.87	33.68	92.04	84.35	80.64	31.57	24.57
	4	-192.34	-217.61	-275.43	49.99	35.82	125.18	91.90	89.52	33.11	27.47
	8	-202.77	-231.72	-305.86	52.99	37.88	160.11	98.62	98.34	34.50	29.44
	14	-217.64	-252.17	-354.40	57.40	40.87	213.36	108.61	111.57	38.49	34.89
	18	-226.59	-265.33	-386.01	60.25	42.82	249.98	113.91	120.60	40.49	37.25

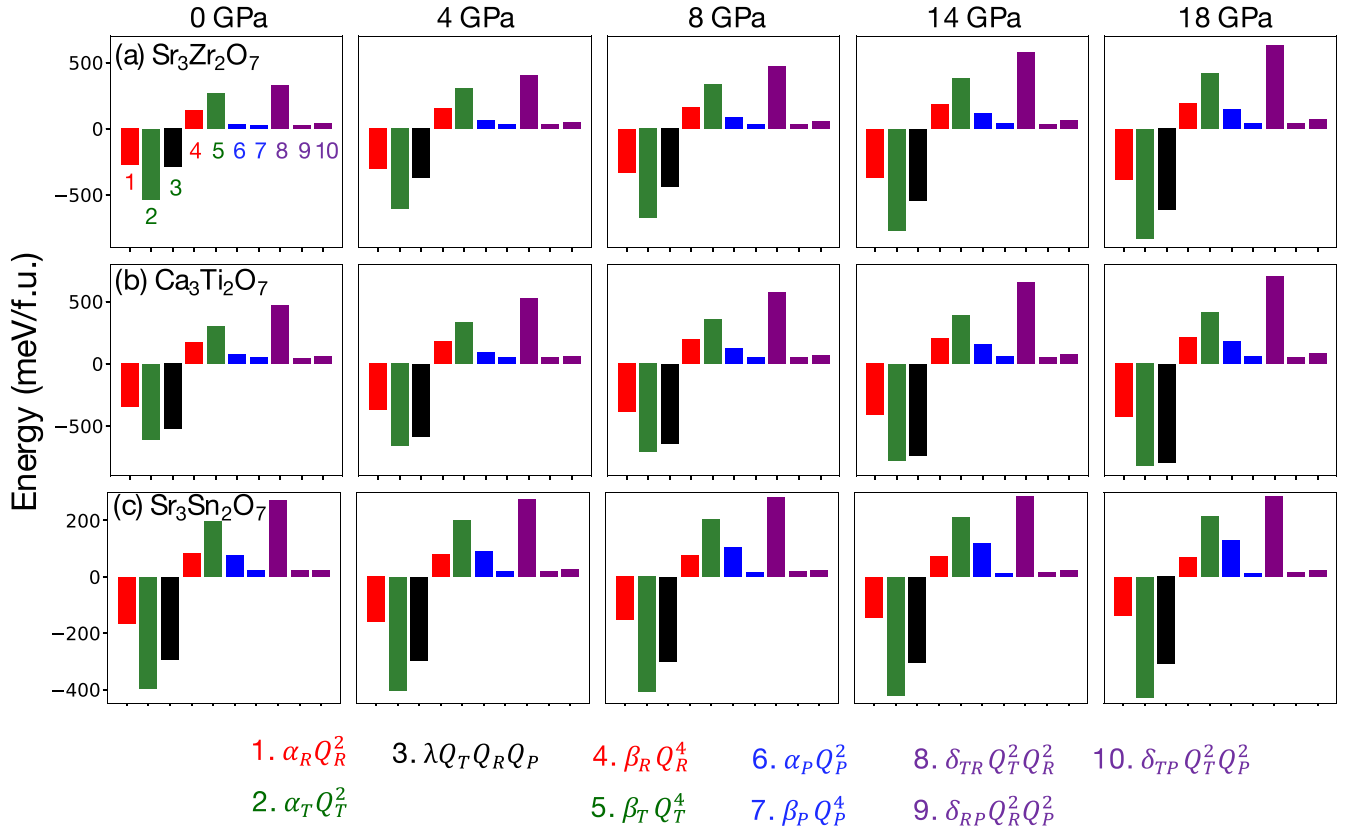


FIG. 12. Energies of the individual terms in the Landau expansion in Eq. (4) for several pressures for (a)  $\text{Sr}_3\text{Zr}_2\text{O}_7$ , (b)  $\text{Ca}_3\text{Ti}_2\text{O}_7$ , and (c)  $\text{Sr}_3\text{Sn}_2\text{O}_7$ . The quadratic and quartic terms involving  $Q_R$ ,  $Q_T$ , and  $Q_P$  are shown in red, green, and blue, respectively. The trilinear coupling term is shown in black and the biquadratic terms are shown in violet. To calculate these energy terms at each pressure, we use the pressure-dependent Landau coefficients from Table V together with the DFT-relaxed distortion amplitudes at that pressure.

compared to the other two compounds:  $E(Q_P)$  increases more than the biquadratic term. This analysis supports the conclusions reached in the main text: that differences in the single-distortion terms  $E(Q_i)$  are primarily responsible to the distinct pressure response of  $\text{Sr}_3\text{Sn}_2\text{O}_7$  compared to the other compounds considered in this work.

#### APPENDIX G: PRESSURE DEPENDENCE OF COUPLING TERMS: A SIMPLIFIED ANALYSIS

In this Appendix we perform a simplified analysis to show the impact of each coupling term in Eq. (4) on the octahedral rotation amplitudes. We start with a single-rotation structure

TABLE VI. Individual Landau energy terms (in meV/f.u.) from Eq. (4) as a function of pressure for  $\text{Sr}_3\text{Zr}_2\text{O}_7$ ,  $\text{Sr}_3\text{Sn}_2\text{O}_7$ , and  $\text{Ca}_3\text{Ti}_2\text{O}_7$ . This data also is presented in Fig. 12.

	$P$ (GPa)	$\alpha_R Q_R^2$	$\alpha_T Q_T^2$	$\lambda Q_T Q_R Q_P$	$\beta_R Q_R^4$	$\beta_T Q_T^4$	$\alpha_P Q_P^2$	$\beta_P Q_P^4$	$\delta_{RT} Q_T^2 Q_R^2$	$\delta_{RP} Q_R^2 Q_P^2$	$\delta_{TP} Q_T^2 Q_P^2$
$\text{Sr}_3\text{Zr}_2\text{O}_7$	0	-276.28	-534.24	-289.75	138.19	267.01	37.46	28.36	328.37	27.10	38.84
	4	-303.76	-606.10	-371.65	151.91	303.05	60.55	33.83	406.16	30.38	47.43
	8	-332.15	-673.95	-440.30	166.00	336.95	83.31	37.57	473.40	32.69	55.27
	14	-367.46	-771.20	-543.26	183.78	385.40	119.43	41.81	577.84	35.99	67.75
	18	-384.98	-831.79	-615.43	192.43	416.09	147.13	45.06	634.48	37.93	71.15
$\text{Sr}_3\text{Sn}_2\text{O}_7$	0	-166.42	-396.61	-293.90	83.15	198.33	76.36	21.70	269.95	23.22	24.01
	4	-159.76	-402.52	-298.00	79.86	201.38	91.23	18.81	275.80	20.54	25.94
	8	-153.37	-408.12	-300.05	76.73	203.28	103.58	16.30	281.23	18.56	24.24
	14	-143.44	-421.58	-304.92	71.72	210.89	119.52	13.42	284.61	15.93	23.10
	18	-136.09	-428.54	-309.59	68.03	213.53	128.61	11.91	286.19	14.43	22.47
$\text{Ca}_3\text{Ti}_2\text{O}_7$	0	-347.37	-610.15	-524.24	173.72	304.94	72.68	52.61	467.09	48.00	58.37
	4	-369.75	-660.81	-583.41	184.75	330.33	96.21	54.28	522.61	48.92	64.11
	8	-388.12	-708.52	-642.76	194.16	354.17	120.82	56.15	575.55	49.82	67.94
	14	-412.37	-778.12	-735.80	206.08	389.16	157.31	59.04	652.29	53.77	79.38
	18	-426.21	-822.48	-794.74	213.16	411.43	181.74	60.21	703.18	55.37	83.95

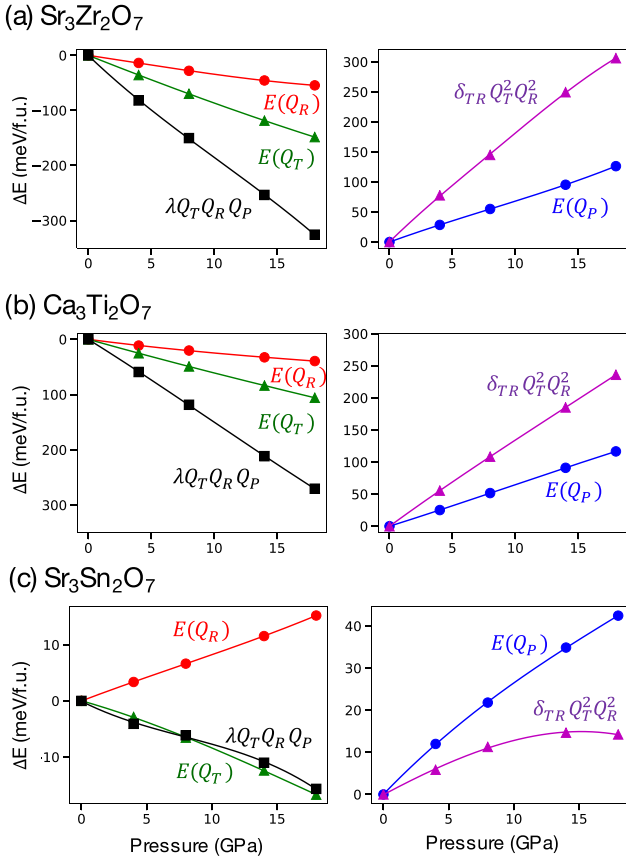


FIG. 13. Energy difference  $\Delta E$  of individual Landau energy terms at pressure  $P$  compared to their value at 0 GPa, for (a)  $\text{Sr}_3\text{Zr}_2\text{O}_7$ , (b)  $\text{Ca}_3\text{Ti}_2\text{O}_7$ , and (c)  $\text{Sr}_3\text{Sn}_2\text{O}_7$ . Here  $E(Q_i) = \alpha_i Q_i^2 + \beta_i Q_i^4$  for  $Q_i = Q_T, Q_R, Q_P$ .

(we choose  $X_2^+$  here as an example) and then add in one coupling term at a time. In this example, we use the pressure-dependent Landau coefficients for  $\text{Sr}_3\text{Zr}_2\text{O}_7$  obtained from Fig. 5.

With only the  $X_2^+$  rotation included, Eq. (4) reduces to

$$E(Q_R) = \alpha_R Q_R^2 + \beta_R Q_R^4, \quad (\text{G1})$$

and the rotation amplitude that minimizes the energy is  $Q_R = \sqrt{-\alpha_R/(2\beta_R)}$ . Figure 14 (red circles) shows this term as a function of pressure:  $Q_R$  initially increases, then becomes flat, and then decreases slightly.

We next add in the biquadratic  $Q_T$ - $Q_R$  coupling. Setting  $Q_T = Q_{T0}$  to a constant value for simplicity (which is reasonable, given its weak pressure dependence), the free energy then becomes

$$\begin{aligned} E(Q_R) &= (\alpha_R + \delta_{RT} Q_{T0}^2) Q_R^2 + \beta_R Q_R^4 \\ &= \alpha'_R Q_R^2 + \beta_R Q_R^4, \end{aligned} \quad (\text{G2})$$

where  $\alpha'_R = \alpha_R + \delta_{RT} Q_{T0}^2$ . The rotation amplitude that minimizes the energy is now  $Q_R = \sqrt{-\alpha'_R/(2\beta_R)}$ . Thus the biquadratic coupling simply renormalizes the second order coefficient to a smaller value, thus reducing  $Q_R$ . This effect is shown in Fig. 14 (blue triangles), where now the pressure response is qualitatively different and  $Q_R$  decreases with in-

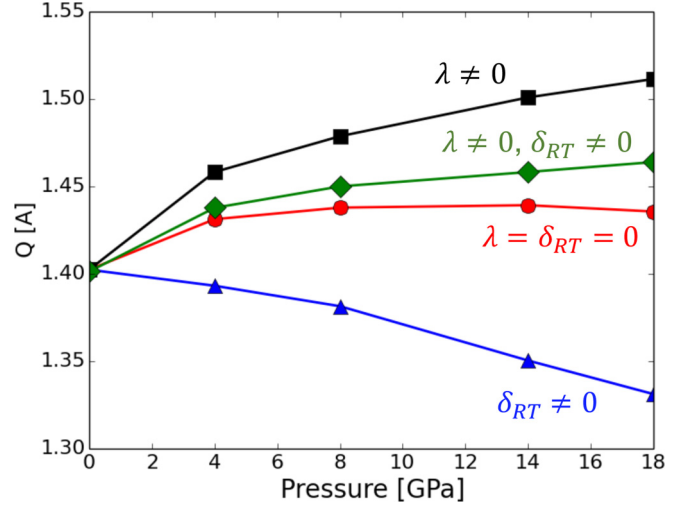


FIG. 14. Amplitude of the  $X_2^+$  rotation ( $Q_R$ ) in  $\text{Sr}_3\text{Zr}_2\text{O}_7$  as a function of pressure computed using Eqs. (G1)–(G4).

creasing pressure (in this example we set  $Q_{T0} = 1.0 \text{ \AA}$ ). Note that for simplicity we set  $\delta_{RP} = \delta_{TP} = 0$  because they are much smaller than  $\delta_{RT}$ .

Next, we consider the trilinear coupling (and neglect the biquadratic coupling by setting  $\delta_{RT} = 0$ ). Setting  $Q_T = Q_{T0}$  and  $Q_P = Q_{P0}$  to fixed values, the free energy now becomes

$$E(Q_R) = \alpha_R Q_R^2 + \beta_R Q_R^4 + \lambda Q_R Q_{T0} Q_{P0}. \quad (\text{G3})$$

Taking the derivative and setting it to zero, we then find

$$Q_R^3 + \frac{\alpha_R}{2\beta_R} Q_R + \frac{\lambda Q_{T0} Q_{P0}}{4\beta_R} = 0. \quad (\text{G4})$$

Setting  $Q_{T0} = Q_{P0} = 1.0 \text{ \AA}$  and solving Eq. (G4) reveals that the inclusion of  $\lambda$  causes  $Q_R$  to increase strongly with pressure, as shown in Fig. 14 (black squares).

Finally, we calculate  $Q_R$  when both coupling terms are included at the same time ( $\lambda \neq 0, \delta_{RT} \neq 0$ ). This is implemented by replacing  $\alpha_R$  with  $\alpha'_R$  in Eq. (G4). Solving yields the result shown in Fig. 14 (green diamonds), where now  $Q_R$  only weakly increases with pressure, and looks similar to the case with no coupling terms.

Thus we see that the near cancellation of the trilinear and biquadratic coupling terms contributes to the small changes in octahedral rotation amplitudes with pressure. In particular, a slightly different balance between the different energetic terms in the different materials leads to the realization of slight increases/decreases in octahedral rotation amplitudes under pressure.

## APPENDIX H: ENTHALPY DIFFERENCES BETWEEN STRUCTURAL PHASES

Figure 15 shows the enthalpy difference  $H(s) - H(A2_1am)$  between candidate high-pressure structural phases ( $s$ ) and  $A2_1am$  for  $\text{Ca}_3\text{Ti}_2\text{O}_7$  and  $\text{Sr}_3\text{Zr}_2\text{O}_7$ . The DFT calculations are performed at  $T = 0$ , so here the enthalpy  $H$  is equal to the Gibbs free energy  $G$ , that is,  $G = H = E + PV$ .

Figure 15(a) shows that the enthalpy difference between all candidate structural phases and  $A2_1am$  remains

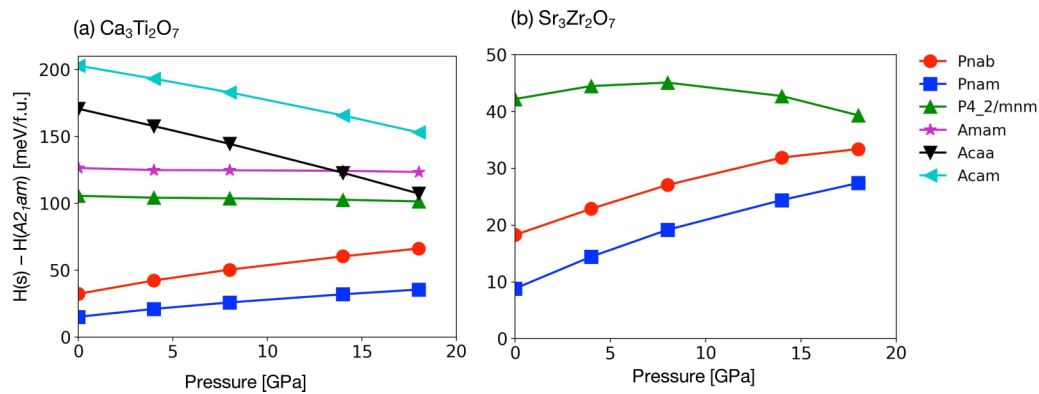


FIG. 15. Enthalpy difference between possible high-pressure structural phases ( $s$ ) and  $A2_1am$  for (a)  $Ca_3Ti_2O_7$  and (b)  $Sr_3Zr_2O_7$ , calculated with DFT.

positive for  $Ca_3Ti_2O_7$  up to 18 GPa. In addition, the enthalpy difference gets more positive with increasing pressure for the lowest enthalpy phases,  $Pnam$  and  $Pnab$ . The enthalpy difference  $H(Acaa) - H(A2_1am)$  decreases with increasing pressure, suggesting there could be a possible transition at a significantly higher pressure. We consider the subset of

lowest enthalpy phases for  $Sr_3Zr_2O_7$  in Fig. 15(b) and observe similar behavior. These results suggest that  $Ca_3Ti_2O_7$  and  $Sr_3Zr_2O_7$  stay in the  $A2_1am$  phase throughout the pressure range considered in this work, although structural phase transitions may be accessible to room temperature experiments at lower pressures.

- [1] P. M. Woodward, *Acta Crystallogr.*, **B 53**, 44 (1997).
- [2] M. Imada, A. Fujimori, and Y. Tokura, *Rev. Mod. Phys.* **70**, 1039 (1998).
- [3] H. W. Eng, P. W. Barnes, B. M. Auer, and P. M. Woodward, *J. Solid State Chem.* **175**, 94 (2003).
- [4] J. M. Rondinelli, S. J. May, and J. W. Freeland, *MRS Bull.* **37**, 261 (2012).
- [5] E. Moon, R. Colby, Q. Wang, E. Karapetrova, C. Schlepütz, M. Fitzsimmons, and S. J. May, *Nat. Commun.* **5**, 5710 (2014).
- [6] P. G. Radaelli, G. Iannone, M. Marezio, H. Y. Hwang, S. W. Cheong, J. D. Jorgensen, and D. N. Argyriou, *Phys. Rev. B* **56**, 8265 (1997).
- [7] J. M. Rondinelli and N. A. Spaldin, *Adv. Mater.* **23**, 3363 (2011).
- [8] N. A. Benedek, A. T. Mulder, and C. J. Fennie, *J. Solid State Chem.* **195**, 11 (2012).
- [9] G. Samara, T. Sakudo, and K. Yoshimitsu, *Phys. Rev. Lett.* **35**, 1767 (1975).
- [10] J. Zhao, N. Ross, and R. Angel, *Acta Crystallogr.*, **B: Struct. Sci.** **60**, 263 (2004).
- [11] R. J. Angel, J. Zhao, and N. L. Ross, *Phys. Rev. Lett.* **95**, 025503 (2005).
- [12] H. J. Xiang, M. Guennou, J. Íñiguez, J. Kreisel, and L. Bellaïche, *Phys. Rev. B* **96**, 054102 (2017).
- [13] B. Magyari-Köpe, L. Vitos, G. Grimvall, B. Johansson, and J. Kollar, *Phys. Rev. B* **65**, 193107 (2002).
- [14] T. Tohei, A. Kuwabara, T. Yamamoto, F. Oba, and I. Tanaka, *Phys. Rev. Lett.* **94**, 035502 (2005).
- [15] V. S. Bhadram, D. Swain, R. Dhanya, M. Polentarutti, A. Sundaresan, and C. Narayana, *Mater. Res. Exp.* **1**, 026111 (2014).
- [16] N. A. Benedek and C. J. Fennie, *Phys. Rev. Lett.* **106**, 107204 (2011).
- [17] S. Yoshida, H. Akamatsu, R. Tsuji, O. Hernandez, H. Padmanabhan, A. Sen Gupta, A. S. Gibbs, K. Mibu, S. Murai, J. M. Rondinelli *et al.*, *J. Am. Chem. Soc.* **140**, 15690 (2018).
- [18] S. Yoshida, K. Fujita, H. Akamatsu, O. Hernandez, A. Sen Gupta, F. G. Brown, H. Padmanabhan, A. S. Gibbs, T. Kuge, R. Tsuji *et al.*, *Adv. Funct. Mater.* **28**, 1801856 (2018).
- [19] S. Liu, H. Zhang, S. Ghose, M. Balasubramanian, Z. Liu, S. G. Wang, Y.-S. Chen, B. Gao, J. Kim, S.-W. Cheong, and T. A. Tyson, *Phys. Rev. B* **99**, 224105 (2019).
- [20] Y. Wang, F.-T. Huang, X. Luo, B. Gao, and S.-W. Cheong, *Adv. Mater.* **29**, 1601288 (2017).
- [21] F.-T. Huang, F. Xue, B. Gao, L. Wang, X. Luo, W. Cai, X.-Z. Lu, J. M. Rondinelli, L. Chen, and S.-W. Cheong, *Nat. Commun.* **7**, 11602 (2016).
- [22] F. Ye, J. Wang, J. Sheng, C. Hoffmann, T. Gu, H. J. Xiang, W. Tian, J. J. Molaison, A. M. dos Santos, M. Matsuda, B. C. Chakoumakos, J. A. Fernandez-Baca, X. Tong, B. Gao, J. W. Kim, and S. W. Cheong, *Phys. Rev. B* **97**, 041112(R) (2018).
- [23] M. H. Lee, C.-P. Chang, F.-T. Huang, G. Y. Guo, B. Gao, C. H. Chen, S.-W. Cheong, and M.-W. Chu, *Phys. Rev. Lett.* **119**, 157601 (2017).
- [24] X. Liu, B. Chen, J. Lu, Z. Hu, and X. Chen, *Appl. Phys. Lett.* **113**, 242904 (2018).
- [25] R. Uppuluri, H. Akamatsu, A. Sen Gupta, H. Wang, C. M. Brown, K. E. Agueda Lopez, N. Alem, V. Gopalan, and T. E. Mallouk, *Chem. Mater.* **31**, 4418 (2019).
- [26] C. F. Li, S. H. Zheng, H. W. Wang, J. J. Gong, X. Li, Y. Zhang, K. L. Yang, L. Lin, Z. B. Yan, S. Dong, and J. M. Liu, *Phys. Rev. B* **97**, 184105 (2018).
- [27] M. S. Senn, C. A. Murray, X. Luo, L. Wang, F.-T. Huang, S.-W. Cheong, A. Bombardi, C. Ablitt, A. A. Mostofi, and N. C. Bristowe, *J. Am. Chem. Soc.* **138**, 5479 (2016).
- [28] X.-Z. Lu and J. M. Rondinelli, *Nat. Mater.* **15**, 951 (2016).



- [29] Y. Zhang, M. P. K. Sahoo, T. Shimada, T. Kitamura, and J. Wang, *Phys. Rev. B* **96**, 144110 (2017).
- [30] Y. S. Oh, X. Luo, F.-T. Huang, Y. Wang, and S.-W. Cheong, *Nat. Mater.* **14**, 407 (2015).
- [31] X. Xu, Y. Wang, F.-T. Huang, K. Du, E. A. Nowadnick, and S.-W. Cheong, *Adv. Funct. Mater.* **30**, 2003623 (2020).
- [32] P. Hohenberg and W. Kohn, *Phys. Rev.* **136**, B864 (1964).
- [33] G. Kresse and J. Furthmüller, *Comput. Mater. Sci.* **6**, 15 (1996).
- [34] P. E. Blöchl, *Phys. Rev. B* **50**, 17953 (1994).
- [35] J. P. Perdew, A. Ruzsinszky, G. I. Csonka, O. A. Vydrov, G. E. Scuseria, L. A. Constantin, X. Zhou, and K. Burke, *Phys. Rev. Lett.* **100**, 136406 (2008).
- [36] H. J. Monkhorst and J. D. Pack, *Phys. Rev. B* **13**, 5188 (1976).
- [37] H. Stokes, D. Hatch, and B. Campbell, ISOTROPY software suite, <http://stokes.byu.edu/isotropy.html>
- [38] K. Momma and F. Izumi, *J. Appl. Crystallogr.* **41**, 653 (2008).
- [39] A. Glazer, *Acta Crystallogr., B* **28**, 3384 (1972).
- [40] V. M. Goldschmidt, *Naturwissenschaften* **14**, 477 (1926).
- [41] A. T. Mulder, N. A. Benedek, J. M. Rondinelli, and C. J. Fennie, *Adv. Funct. Mater.* **23**, 4810 (2013).
- [42] M. W. Lufaso and P. M. Woodward, *Acta Crystallogr., B: Struct. Sci.* **57**, 725 (2001).
- [43] I. D. Brown, *Chem. Soc. Rev.* **7**, 359 (1978).
- [44] N. A. Benedek and C. J. Fennie, *J. Phys. Chem. C* **117**, 13339 (2013).
- [45] E. A. Nowadnick and C. J. Fennie, *Phys. Rev. B* **94**, 104105 (2016).
- [46] F.-T. Huang, B. Gao, J.-W. Kim, X. Luo, Y. Wang, M.-W. Chu, C.-K. Chang, H.-S. Sheu, and S.-W. Cheong, *npj Quantum Mater.* **1**, 1 (2016).
- [47] M. J. Pitcher, P. Mandal, M. S. Dyer, J. Alaria, P. Borisov, H. Niu, J. B. Claridge, and M. J. Rosseinsky, *Science* **347**, 420 (2015).
- [48] H. Nakano, N. Ishizawa, and N. Kamegashira, *J. Eur. Ceram. Soc.* **30**, 233 (2010).
- [49] H. Wang, G. Gou, and J. Li, *Nano Energy* **22**, 507 (2016).
- [50] T. Gu, T. Scarbrough, Y. Yang, J. Íñiguez, L. Bellaiche, and H. J. Xiang, *Phys. Rev. Lett.* **120**, 197602 (2018).
- [51] E. I. Paredes Aulestia, Y. W. Cheung, Y.-W. Fang, J. He, K. Yamaura, K. T. Lai, S. K. Goh, and H. Chen, *Appl. Phys. Lett.* **113**, 012902 (2018).
- [52] K. A. Smith, S. P. Ramkumar, N. C. Harms, A. J. Clune, X. Xu, S.-W. Cheong, Z. Liu, E. A. Nowadnick, and J. L. Musfeldt, *Phys. Rev. B* **104**, 064106 (2021).